

Constraining the role of star cluster mergers in nuclear cluster formation: simulations confront integral-field data

Markus Hartmann,¹^{*} Victor P. Debattista,¹[†] Anil Seth,²[‡] Michele Cappellari³^{*}
and Thomas R. Quinn⁴^{*}

¹Jeremiah Horrocks Institute, University of Central Lancashire, Preston PR1 2HE

²Harvard–Smithsonian Center for Astrophysics, 60 Garden Street Cambridge, MA 02138, USA

³Sub-department of Astrophysics, University of Oxford, Denys Wilkinson Building, Keble Road, Oxford OX1 3RH

⁴Astronomy Department, University of Washington, Box 351580, Seattle, WA 98195, USA

Accepted 2011 August 18. Received 2011 August 17; in original form 2011 March 24

ABSTRACT

We present observations and dynamical models of the stellar nuclear clusters (NCs) at the centres of NGC 4244 and M33. We then compare these to an extensive set of simulations testing the importance of purely stellar dynamical mergers on the formation and growth of NCs. Mergers of star clusters are able to produce a wide variety of observed properties, including densities, structural scaling relations, shapes (including the presence of young discs) and even rapid rotation. None the less, difficulties remain, most notably that the second-order kinematic moment $V_{\text{rms}} = \sqrt{V^2 + \sigma^2}$ of the models is too centrally peaked to match observations. This can be partially remedied by the merger of star clusters on to a pre-existing nuclear disc, but the line-of-sight velocity V is still more slowly rising than in NGC 4244. Our results therefore suggest that purely stellar dynamical mergers cannot form NCs and that gas dissipation is a necessary ingredient for at least ~ 50 per cent of a NC's mass. The negative vertical anisotropy found in NGC 4244, however, requires at least 10 per cent of the mass to have been accreted as stars, since gas dissipation and *in situ* star formation leads to positive vertical anisotropy.

Key words: galaxies: evolution – galaxies: kinematics and dynamics – galaxies: structure.

1 INTRODUCTION

Studies of the centres of galaxies across the Hubble sequence have shown that they frequently host central massive objects (CMOs) such as supermassive black holes (SMBHs) and massive stellar nuclear clusters (NCs). NCs are very common: the Advanced Camera for Surveys (ACS) Virgo Cluster Survey found a NC in 66–88 per cent of low- and intermediate-luminosity early-type galaxies (Grant, Kuipers & Phillipps 2005; Côté et al. 2006). A similar fraction, ~ 75 per cent, of late-type spiral galaxies contain a NC (Böker et al. 2002). However, NCs do not appear to populate the most massive early-type galaxies brighter than $M_B \approx -20.5$ (Grant et al. 2005; Côté et al. 2006). Both Rossa et al. (2006) and Côté et al. (2006) found that the luminosity of the NC correlates with that of the host galaxy in elliptical and early-type spiral galaxies. Remark-

ably, both NCs and SMBHs follow the same correlation between their mass, M_{CMO} , and that of their host galaxy, with NCs on the lower end and SMBHs on the upper end of the relation (Ferrarese et al. 2006b; Wehner & Harris 2006; Li, Haiman & Mac Low 2007). Likewise, both NC and SMBH masses follow an $M_{\text{CMO}}-\sigma_e$ relation with the velocity dispersion of their host spheroid (Ferrarese et al. 2006b; Wehner & Harris 2006), with the relation for NCs parallel to, but ~ 10 times more massive at a given σ_e , that for SMBHs. These observational facts suggest that SMBHs and NCs share a similar growth history (McLaughlin, King & Nayakshin 2006). This motivates us to understand SMBH growth by using the formation of NCs as their visible proxies. An important advantage of NCs is that there are additional observables which can be measured for them, in addition to their mass. In particular, one can characterize their kinematics and stellar population. This provides further constraints to their formation, which we exploit in this paper.

Two main scenarios have been proposed to explain the formation of NCs. One scenario relies on NCs forming *in situ* out of gas falling into the centre. A number of mechanisms have been proposed for driving gas to galactic centres, including the magnetorotational instability (Milosavljević 2004), gas cloud mergers (Bekki 2007) or the action of instabilities (Shlosman & Begelman 1989;

*E-mail: mhartmann@uclan.ac.uk (MH); vpdebattista@uclan.ac.uk (VPD); aseth@cfa.harvard.edu (AS); cappellari@astro.ox.ac.uk (MC); trq@astro.washington.edu (TRQ)

†RCUK Fellow.

‡CfA Fellow.

Maciejewski et al. 2002; Schinnerer, Böker & Meier 2003; Schinnerer et al. 2008). Alternatively, NCs may form from the merging of star clusters (SCs) after sinking to the centre under the action of dynamical friction (Tremaine, Ostriker & Spitzer 1975; Miocchi et al. 2006). Indeed, Lotz et al. (2001) found a depletion of bright globular clusters (GCs) within the inner region of dwarf ellipticals (dEs) and similar colours for the GC and NC population which, however, are bluer than the underlying stellar population of the host. Analysis of NC colours in dE galaxies by Lotz, Miller & Ferguson (2004) and Côté et al. (2006) suggests that many, but not all, dE nuclei could be explained by a cluster merger scenario. Self-consistent simulations have found that mergers can occur, and the resulting NC masses and sizes are consistent with those observed (Bekki et al. 2004; Capuzzo-Dolcetta & Miocchi 2008a,b).

NC formation in late-type galaxies is an ongoing process, with star formation histories that are extended, possibly constant (Rossa et al. 2006; Walcher et al. 2006; Seth et al. 2010), and stars younger than 100 Myr present. Mergers and accretion of *old* SCs is thus not a viable formation scenario, regardless of whether enough such SCs are available.

However, mergers and accretion of young SCs formed near the centres of galaxies, such as those observed in the Milky Way (Figer, McLean & Morris 1999; Figer et al. 2002), NGC 2139 (Andersen et al. 2008) and NGC 253 (Kornei & McCrady 2009), could still provide a viable formation mechanism. Agarwal & Milosavljević (2011) used analytic modelling to show that infalling SCs from an empirical SC population produce NCs of the right mass in isolated spheroidal and late-type galaxies. Such SCs must form quite close to the galaxy centres ($\lesssim 1$ kpc), otherwise the time-scales for infall due to dynamical friction are prohibitively long (Milosavljević 2004). In a sample of observed bulgeless spiral galaxies, Neumayer et al. (2011) find that the dynamical friction time-scales are < 2 Gyr for SCs with masses $> 2 \times 10^5 M_{\odot}$ within 500 pc. The supply of young SCs to the inner regions may be enhanced because tidal forces are compressive within 10 per cent of the effective radius when the density profile has a Sérsic index $n < 2$ (Emsellem & van de Ven 2008). However, a galaxy with a constant density dark matter core would inhibit infall altogether (Read et al. 2006; Goerdt et al. 2008, 2010).

The morphology and kinematics of NCs in disc galaxies provide additional constraints on their formation. From observations of edge-on galaxies, Seth et al. (2006) find that their NCs are typically elongated along the plane of the galaxy disc. These NCs are often compound structures, with a younger, bluer thin disc [NC disc (NCD)] embedded within an older spheroidal component [NC spheroid (NCS)]. In the case of the NC in NGC 4244, spectra reveal young (< 100 Myr) stars in the NCD amounting to ~ 5 per cent of the total NC mass. Furthermore, integral-field spectroscopy of this NC shows rotation in the same sense as the galaxy (Seth et al. 2008b). As we show below, it is not yet possible to determine whether this rotation is restricted to the NCD.

Accretion without gas dissipation need not result in slowly rotating systems: Read et al. (2008) showed that satellite galaxies that accrete on to disc galaxies can get dragged down on to the plane of the disc and settle directly into a rapidly rotating thick disc with $(V/\sigma)_{*}$ as large as 4. Likewise, Eliche-Moral et al. (2006) find that low-density satellites can accrete on to bulges and end up rapidly rotating. Can NCDs form through an analogous process? Since SCs falling into the nucleus are likely to have formed in the mid-plane of the galaxy, they will generally share in its rotation.

In this paper, we explore in detail whether the SC merger/accretion scenario is able to produce the density and kine-

matic properties observed in NCs. Therefore, we neglect gas dynamics and the effects of stellar evolution, such as stellar winds and supernova feedback, in our simulations. The half-mass relaxation time for the NC in NGC 4244, with $R_{\text{eff}} \simeq 5$ pc and total mass $1.1 \times 10^7 M_{\odot}$ is ~ 10 Gyr. NCs in the ACS Virgo Cluster Survey have relaxation times ranging from 1 to 10 Gyr (Merritt 2009). Therefore, it is reasonable to approximate NCs as collisionless systems on time-scales of $\lesssim 1$ Gyr, allowing us to use standard collisionless N -body codes to simulate their evolution. In Section 2, we present the observations of the NCs in NGC 4244 and M33. In Section 3, we model integral-field data of NGC 4244 and M33 using the Jeans Anisotropic Multi-Gaussian Expansion (MGE) method of Cappellari (2008). In Section 4, we describe our simulations and methods. We present the results of NCs formed by mergers/accretions of SCs in Section 5. In Section 6, we introduce an initial NCD and follow its evolution as it accretes SCs. In Section 7, we apply the Jeans Anisotropic MGE (JAM) modelling also to the simulations. We discuss the implications of our simulations and show that a purely collisionless merger origin of NCs is not consistent with the observations in Section 8.

2 OBSERVATIONAL CONSTRAINTS

We compare our simulations with observations of the NCs in two nearby galaxies, M33 and NGC 4244. These two galaxies provide us with well-resolved nuclei for which integral-field kinematic data are available. While M33 is inclined by $i = 49^{\circ}$ (Corbelli & Schneider 1997), NGC 4244 is an edge-on galaxy. These two objects thus give us two different perspectives for studying the morphology and kinematics of NCs in disc galaxies. In this paper, we assume a distance of 4.4 Mpc for NGC 4244 (Seth, Dalcanton & de Jong 2005) and 0.8 Mpc for M33 (Lauer et al. 1998).

2.1 Spectroscopy of NGC 4244 and M33

Seth et al. (2006) presented *Hubble Space Telescope F814W* photometry of the NC in NGC 4244, which is resolved into a NCS and a bluer NCD. The half-mass radius, R_{eff} , of the NC obtained by fitting a King profile to the ACS/*F814W* images (Seth et al. 2006) is about 5 pc.

Here we use K -band spectra of NGC 4244 (Seth et al. 2008b) and M33 (Seth et al., in preparation) obtained at Gemini North with the Near-Infrared Integral Field Spectrograph (NIFS), an image slicing field unit spectrograph. The point spread function (PSF) core in both observations is ~ 0.1 arcsec full width at half-maximum (FWHM), with final data cubes sampled with 0.05 arcsec pixel $^{-1}$. In NGC 4244, this corresponds to 1.06 pc pixel $^{-1}$, while in M33 the pixel scale is 0.19 pc pixel $^{-1}$. The line-of-sight velocities are determined by the fitting method penalized pixel fitting (pPXF) of Cappellari & Emsellem (2004). The code uses a Gauss–Hermite parametrization up to h3–h4 (Gerhard 1993; van der Marel & Franx 1993) to fit the line-of-sight velocities. The imperfect adaptive optics corrections result in nearly half of the light being scattered into a PSF halo (~ 0.7 arcsec FWHM). This leads to problems separating the rotation in the NCS and NCD in NGC 4244 (see Section 3.2). In both clusters, the rotation amplitude increases with radius out to the effective radius, and decreases at larger radii. However, whether or not a NCD is present in the NC of M33 cannot be determined because of the galaxy’s inclination. In Fig. 1, we show the line-of-sight velocity profiles of M33 and NGC 4244.

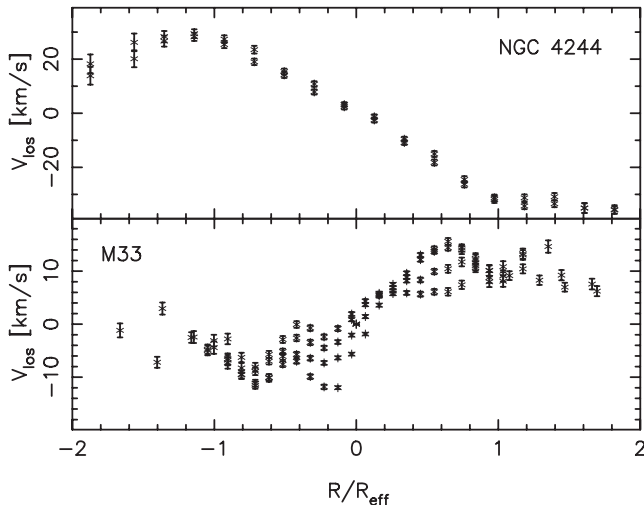


Figure 1. Profiles from the NIFS data (Seth et al. 2008b) of line-of-sight velocities along the major axis in NGC 4244 (top) and M33. The kinematics were extracted from the integral-field data within a slit of $|z| < 0.4$ pc. This corresponds to $0.08R_{\text{eff}}$ for NGC 4244 and $0.2R_{\text{eff}}$ for M33.

2.2 Isophotal shape of the NC in NGC 4244

The shape of an isophote can be quantified by the Fourier coefficients of the expansion

$$I(\phi) = I_0 + \sum_{n=1}^{\infty} A_n \sin(n\phi) + B_n \cos(n\phi), \quad (1)$$

where I_0 is the mean intensity along the ellipse, ϕ is the azimuthal angle and $A_n, B_n (n = 1, 2, \dots)$ are harmonic amplitudes. The ellipse which best fits the isophote has the coefficients $A_n, B_n (n = 1, 2)$ equal to zero. The deviations from the best-fitting isophote are then given by the higher order coefficients $A_n, B_n (n = 3, 4, \dots)$. The leading residual term generally will be the $n = 4$ term, which determines whether the isophote is discy ($B_4 > 0$) or boxy ($B_4 < 0$). We use the task ELLIPSE in IRAF¹ to measure B_4 . The task ELLIPSE reads a 2D image and uses an iterative method described by Jedrzejewski (1987) to fit elliptical isophotes. The parameter B_4 has been shown to correlate with kinematic properties of the host galaxy in observations (Bender 1988; Kormendy & Djorgovski 1989; Kormendy & Bender 1996) and in simulations of galaxy mergers (Naab, Burkert & Hernquist 1999; Naab & Burkert 2003; Naab, Khochfar & Burkert 2006). This result was strongly confirmed with the large ATLAS^{3D} sample of early-type galaxies (Cappellari et al. 2011) which demonstrated that a significant disciness is an unambiguous indication of a fast rotator galaxy (Emsellem et al. 2011). Fig. 2 shows B_4 for the NC in NGC 4244, which is clearly discy.

2.3 Axisymmetry of the M33 nucleus

The face-on axial symmetry is an important constraint on the formation of any stellar system. In general, the merger of stellar systems leads to triaxial systems, e.g. elliptical galaxies are found to be triaxial (Wagner, Bender & Moellenhoff 1988; Naab, Burkert & Hernquist 1999; Naab & Burkert 2003; Naab, Khochfar & Burkert 2006). Very little data are available for the face-on axial symmetry of NCs. For the NC in M33, we find evidence for axisymmetry. The inner 0.5 arcsec ($=1.8$ pc) of the NC in M33 has an apparent $b/a =$

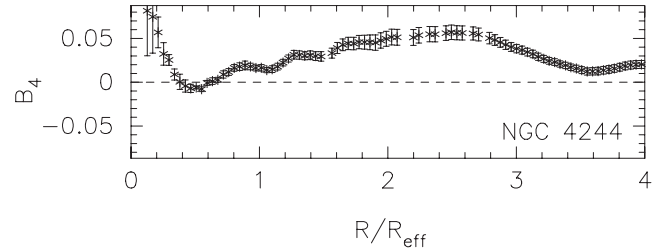


Figure 2. B_4 for the NC in NGC 4244 derived from the integrated K -band flux data (Seth et al. 2008b).

0.84, with an average position angle (PA) $= 19^\circ 3$ (Lauer et al. 1998), which is close to the PA of the inner disc PA $= 23^\circ \pm 1^\circ$ within $R < 4.0$ kpc (Zaritsky, Elston & Hill 1989). Thus we can assume that the NC is in the same plane as the inner disc, and therefore it is possible to determine the NC's apparent axial ratio b/a . The galaxy is inclined by $i = 49^\circ$ (Corbelli & Schneider 1997), so that an oblate spheroid of apparent axial ratio b/a at an inclination i would have an intrinsic vertical-to-horizontal axial ratio q_0 given by

$$q_0 = \sqrt{\frac{(b/a)^2 - \cos^2 i}{\sin^2 i}} \quad (2)$$

(Hubble 1926). The $q_0 \simeq 0.7$ that equation (2) implies for M33's NC is fully consistent with the range of values of q_0 found in edge-on galaxies by Seth et al. (2006) (NGC 4244 having $q_0 \sim 0.5$). Moreover, we measured the kinematical PA_{kin} $= 36^\circ \pm 18^\circ$ (1σ error) from the NIFS integral-field kinematics, with the routine FIT_KINEMATIC_PA described in appendix C of Krajnović et al. (2006). Thus the kinematical misalignment is consistent with zero, consistent with the NC of M33 being axisymmetric.

3 MODELLING THE OBSERVATIONS

We want to compare the kinematics of the observed NCs to those of the simulations. Given that integral-field kinematics are available for the observed NCs, we use two methods which make full use of the 2D data. One method is based on the Jeans equations and the other is based on the $(V/\sigma, \epsilon)$ diagram. In the following, we show that consistent results are obtained with both approaches.

3.1 The Jeans Anisotropic MGE dynamical models

The integral-field stellar kinematics for the NCs in NGC 404 (Seth et al. 2010), NGC 4244 (Seth et al. 2006) and M33 (Seth et al., in preparation), the few NCs for which this type of data are available, suggest that NCs are likely not far from oblate axisymmetric systems (as we also argued in Section 2.3). A classic reference model to quantify the rotation of axisymmetric galaxies is the *isotropic rotator* (Binney 1978), to which real galaxies have often been compared (e.g. Satoh 1980; Binney, Davies & Illingworth 1990; van der Marel 1991; van der Marel & van Dokkum 2007; van der Wel & van der Marel 2008).

Recent dynamical modelling studies have found that real axisymmetric galaxies are generally best matched by models which have a nearly oblate velocity ellipsoid, flattened along the direction of the symmetry axis $\sigma_z \lesssim \sigma_R \approx \sigma_\phi$ (Cappellari et al. 2007; Cappellari 2008; Thomas et al. 2009). A useful generalization of the isotropic rotator to quantify the rotation of these anisotropic systems is then a *rotator with oblate velocity ellipsoid* ($\sigma_z \leq \sigma_R = \sigma_\phi$), which provides a good approximation for the observed integral-field kinematics of real galaxies (Cappellari 2008; Scott et al. 2009).

¹ <http://iraf.noao.edu/iraf/web/>

To perform the measurement of the degree of rotation we used the Jeans Anisotropic MGE (JAM) software² which implements an efficient solution of the Jeans equations with oblate velocity ellipsoid (Cappellari 2008). Under that assumption, the model gives a unique prediction for the observed first two velocity moments V and $V_{\text{rms}} = \sqrt{V^2 + \sigma^2}$, where V is the observed mean stellar velocity and σ is the mean stellar velocity dispersion.

The luminous matter likely dominates in the high-density nuclei of the studied galaxies. The same is true by construction for the simulations. For this reason, the dynamical models assume that light traces mass. To parametrize the surface brightness distribution of either the galaxies or the N -body simulations, we adopted a MGE (Emsellem, Monnet & Bacon 1994), which we fit to the images with the method and software² of Cappellari (2002). For a given inclination, the models then have one free non-linear parameter, the anisotropy $\beta_z = 1 - \sigma_z^2/\sigma_R^2$ and two linear scaling factors: (i) the dynamical mass-to-light ratio (M/L) and (ii) the amount of rotation $\kappa \equiv L_{\text{obs}}/L_{\text{obl}}$, which is the ratio between the observed projected angular momentum L_{obs} and the one for a model with oblate velocity ellipsoid L_{obl} (see Cappellari 2008, for details). To find the best-fitting model parameters, we constructed a grid in the non-linear parameter β_z , and for each value we linearly scaled the M/L to match the V_{rms} data in a χ^2 sense. At the best-fitting (β_z , M/L), we then computed the model velocity V , further assuming $\sigma_R = \sigma_\phi$, and measure the amount of rotation κ from the observed velocity.

3.2 JAM models of observed NCs

We applied the procedure to model the Gemini NIFS stellar kinematics of the NC in NGC 4244 (Seth et al. 2008b). The MGE fit to the nuclear part of the ACS/*F814W* image is shown in Fig. 3. We used the ACS/*F814W* image for the MGE fit, because of the better known PSF compared to the K -band NIFS data. The NC was assumed to be a dynamically distinct component, in equilibrium in the combined potential due to the galaxy and the NC itself. We used all MGE Gaussians, of both the NC and the main galaxy disc, in the calculation of the gravitational potential, but only the nuclear Gaussians were used to parametrize the surface brightness of the NC. Thus our JAM models of NCs are not self-consistent. Although this assumption is physically motivated and can sometimes produce significant differences in the kinematics of the model, in this case, the results are indistinguishable from a self-consistent model. The best-fitting JAM model for NGC 4244, which has an edge-on inclination ($i = 90^\circ$), is shown in Fig. 4. It has a best-fitting anisotropy parameter $\beta_z = -0.2 \pm 0.1$ and a rotation parameter $\kappa = 0.99 \pm 0.05$. This implies that the NC rotates almost perfectly as the reference rotator with oblate velocity ellipsoid (for which $\kappa = 1$). The best-fitting JAM model has no central intermediate-mass black hole (IMBH). However, from our NIFS data we can place an upper limit of $M_\bullet \lesssim 1 \times 10^5 M_\odot$ on the mass of a possible IMBH inside the NC. This is $\lesssim 1$ per cent of the mass of the cluster, $M_{\text{NC}} = (1.1 \pm 0.2) \times 10^7 M_\odot$. For larger M_\bullet , the model shows a clear central peak in V_{rms} which is strongly excluded by the data.

The NC of NGC 4244 is composed of a NCD and a NCS (Seth et al. 2006), which have distinct stellar populations (Seth et al. 2008b). While Seth et al. (2008b) argued that both the disc and spheroid are rotating due to the change of line strengths and optical

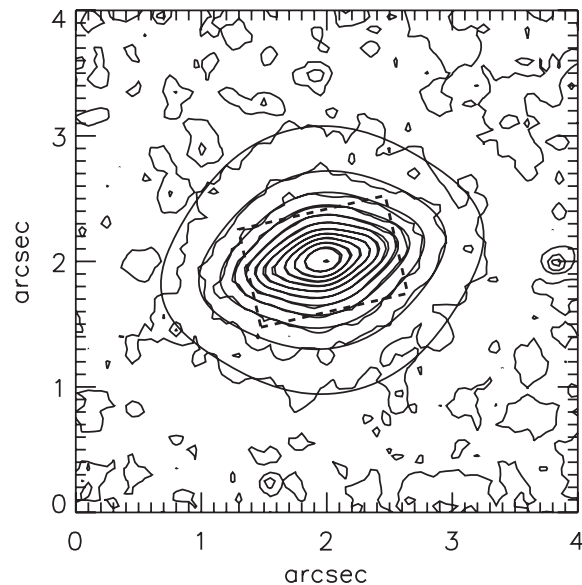


Figure 3. The contours of the surface brightness of the ACS/*F814W* image of the NC in NGC 4244 are overlaid on the PSF-convolved MGE model. The innermost contour corresponds to a surface brightness of $1.8 \times 10^3 L_\odot \text{pc}^{-2}$, while additional contours are in steps of 0.5 mag, with the faintest level corresponding to $1.8 \times 10^3 L_\odot \text{pc}^{-2}$. Both the NCD and the NCS are well described by the model. The scale is $\sim 21.1 \text{ pc arcsec}^{-1}$ with a half-mass radius $\simeq 0.27 \text{ arcsec}$ (Seth et al. 2008b). The dashed box shows the region within which kinematic data are observed.

colour, the models suggest that the rotation signal may come only from the disc. For this, we fitted two MGE models separately for the spheroidal and disc component defined by Seth et al. (2006). We computed the best-fitting JAM model for the V_{rms} like before, but then we fitted V by setting the rotation to zero ($\kappa = 0$) for the MGE Gaussians describing the NCS. This model with an unrotating NCS reproduces the NIFS data as well as the model with constant anisotropy and rotation for both the NCS and the NCD. This is because the flat disc component of the NC dominates the light and the rotation of the model in the region where NIFS data are available. More spatially resolved/extended kinematics would be required to measure the rotation of the spheroidal component of the NC.

We constructed a similar MGE model for the NC of M33 using the Wide Field Planetary Camera 2 (WFPC2) *F814W* photometry. For the JAM model, we adopted the inclination of the main galaxy disc ($i \approx 49^\circ$; Corbelli & Schneider 1997). In this case, the observed distribution of stellar σ from the NIFS data is quite irregular and presents significant asymmetries, which cannot be reproduced by an axisymmetric model. The irregularity in the velocity field is possibly due to granularity in the velocity field, with individual bright asymptotic giant branch stars having significant influence on the velocity and dispersion measurements. The velocity field of M33 and other nearby NCs will be discussed in more detail in an upcoming paper (Seth et al., in preparation). As the anisotropy cannot be reliably inferred from the data, we assumed isotropy and derived the dynamical M/L from a fit to the observed V_{rms} . The rotation parameter derived from the observed V is then $\kappa = 1.02 \pm 0.10$, which, as for NGC 4244, is consistent with the rotation of the reference rotator with oblate velocity ellipsoid. The total mass of the NC is $M_{\text{NC}} = (1.4 \pm 0.2) \times 10^6 M_\odot$.

² Available from <http://purl.org/cappellari/idl/>

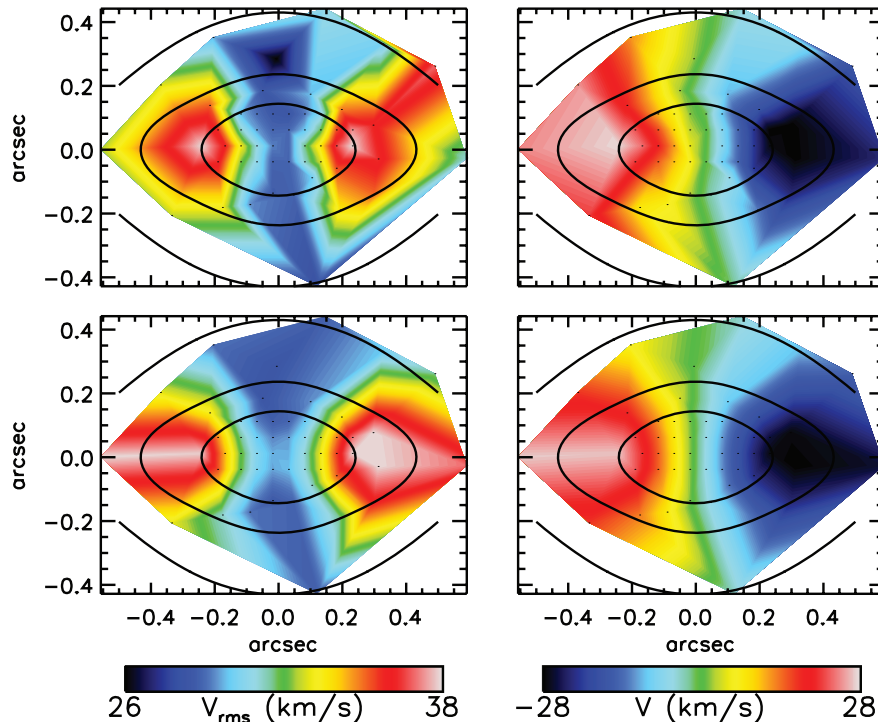


Figure 4. JAM model for the stellar kinematics of NGC 4244. The top two panels show the bisymmetrized NIFS V_{rms} (left) and V (right). The two bottom panels show the corresponding kinematics of the best-fitting JAM model. The contours of the surface brightness are overlaid in steps of 0.5 mag. The dots indicate the position of the centroids of the Voronoi bins for which the kinematics were extracted. The best-fitting model has $\beta_z = -0.2 \pm 0.1$ and $\kappa = 0.99 \pm 0.05$. The NC of NGC 4244 has an almost perfectly oblate velocity ellipsoid.

3.3 Rotation from the $(V/\sigma, \varepsilon)$ diagram

An alternative classic way of quantifying rotation is given by the $(V/\sigma, \varepsilon)$ diagram (Illingworth 1977; Binney 1978). Traditionally, the observed V/σ was quantified from the central velocity dispersion and the maximum rotational velocity. Binney (2005) updated and improved the formalism to compute the quantity in a more robust way when integral-field data are available. Here the availability of integral-field kinematics for both the observations and the simulations allow us to apply this improved method. We use the updated formulae and define

$$\left(\frac{V}{\sigma}\right)_e^2 \equiv \frac{\langle V^2 \rangle}{\langle \sigma^2 \rangle} = \frac{\sum_{n=1}^N F_n V_n^2}{\sum_{n=1}^N F_n \sigma_n^2}, \quad (3)$$

which we applied within $2R_{\text{eff}}$ as a luminosity-weighted quantity, which we estimate from the integral-field kinematics. Here F_n is the flux contained inside the n th Voronoi bin and V_n and σ_n the corresponding measured mean line-of-sight velocity and velocity dispersion. The ellipticity is defined following Cappellari et al. (2007) by a similar expression as

$$(1 - \varepsilon)^2 = q^2 = \frac{\langle y^2 \rangle}{\langle x^2 \rangle} = \frac{\sum_{n=1}^N F_n y_n^2}{\sum_{n=1}^N F_n x_n^2}, \quad (4)$$

where the (x, y) coordinates are centred on the galaxy nucleus and the x axis is aligned with the NC photometric major axis. We estimate ε from the individual pixels, inside a given galaxy isophote, within the same region used for the computation of $(V/\sigma)_e$. The main disadvantage of the $(V/\sigma, \varepsilon)$ diagram, with respect to the JAM models, is that it does not rigorously take account of multiple photometric systems, like a disc and a spheroid. Moreover, while

the diagram can quantify the anisotropy, it does not provide any information on whether it is mostly radial or tangential. Still the diagram provides an important independent test of more detailed models and provides an easy way of comparing simulations and observations.

We used equations (3) and (4) to place the NC of M33 and NGC 4244 on the $(V/\sigma, \varepsilon)$ diagram, using our NIFS data in Fig. 5. In the kinematic extraction with pPXF, we adopt as mean line-of-sight velocity V the peak of the Gaussian, not the first moment computed as integral of the line-of-sight velocity distribution (LOSVD). For the simulations, we compute the mean line-of-sight velocity as the first moment of the particle velocities. Given that the diagram is defined for edge-on orientations, while M33 has an inclination of $i \approx 49^\circ$, we projected the $(V/\sigma, \varepsilon)$ values for the NC to an edge-on view following Binney & Tremaine (2008). The NC in NGC 4244 is seen at a nearly edge-on orientation and is weakly anisotropic. The location of M33 is slightly more uncertain, given the non-edge-on view, but the NC is consistent with isotropy.

4 NUMERICAL METHODS

In this section, we describe the N -body initial conditions for the simulations. We are interested in the evolution at the inner ~ 100 pc region of such galaxies. Assuming a Navarro–Frenk–White halo (Navarro, Frenk & White 1996) with $c \sim 10$ and $M_h \sim 10^{12} M_\odot$, the dark matter mass fraction within this radius is only 20 per cent if the disc is an exponential disc with a scalelength $R_d \sim 2$ kpc and a mass $M_d \sim 4 \times 10^{10} M_\odot$. If instead a bulge of $M_b \sim 1 \times 10^{10} M_\odot$, $n \sim 2$ and $R_{\text{eff}} \sim 0.6$ pc is present, then the dark matter mass fraction is even lower, 1 per cent.

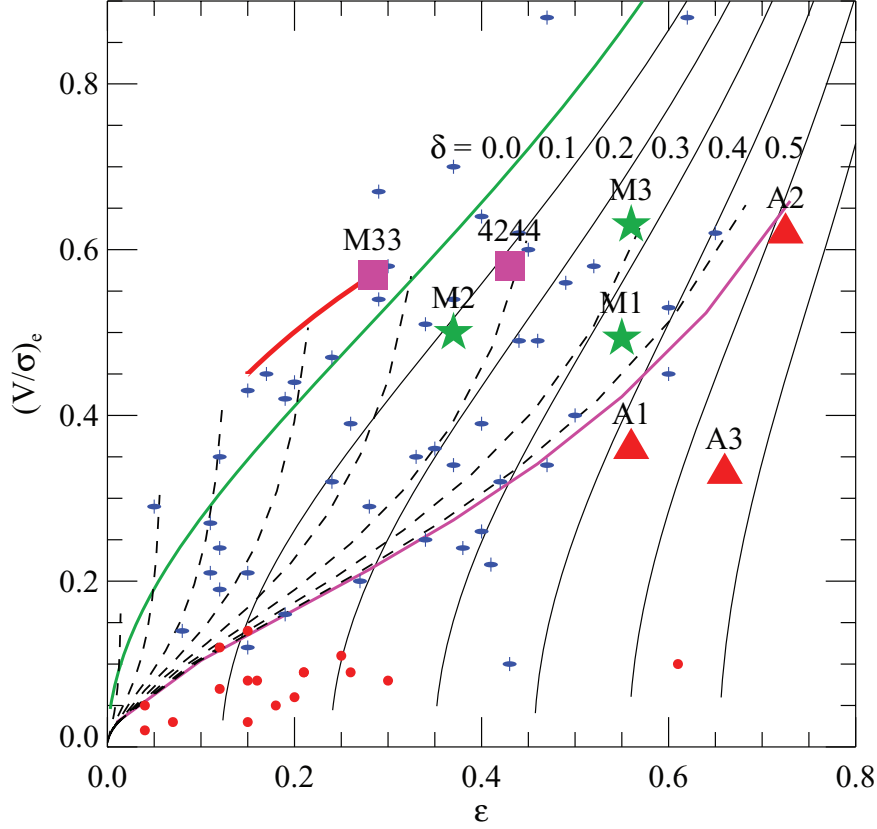


Figure 5. Real and simulated NCs on the $(V/\sigma, \epsilon)$ diagram of Binney (2005). The green line indicates the location of edge-on oblate isotropic models. The black solid lines are oblate anisotropic models, with global anisotropy $\delta \equiv 1 - 2\sigma_z^2/(\sigma_R^2 + \sigma_\phi^2)$ indicated by the labels. The magenta line is the edge-on empirical relation $\delta = 0.7\epsilon$, which describes the lower envelope of the location where fast rotator galaxies are found (see fig. 11 of Cappellari et al. 2007). The dashed lines show how the magenta line transforms when the system is seen at lower inclinations in steps of 10° . The green stars and red triangles indicate the location of the simulated NCs, while the magenta squares are the observed NCs. The observed location for M33 has been projected (red line) assuming an inclination of $i = 49^\circ$. For comparison, we also plot as blue symbols with vertical axes and red filled circles the observed fast and slow rotator early-type galaxies, respectively, from Cappellari et al. (2007). The simulated models M1–M3 and real NCs overlap with the distribution of fast rotator galaxies, while models A1–A3 have somewhat larger anisotropy.

4.1 Galactic disc model

NGC 4244 and M33 are late-type, bulgeless galaxies. We consider only the main galactic disc and adopt an exponential profile:

$$\rho(R, z) = \frac{M_d}{2\pi R_d^2} e^{-R/R_d} \frac{1}{\sqrt{2\pi}z_d} e^{-z^2/2z_d^2}, \quad (5)$$

where M_d is the disc mass, R_d is the scalelength of the disc and z_d the scaleheight. We use $M_d = 10^{10} M_\odot$, $R_d = 2.0$ kpc, $z_d = 200$ pc and truncate the disc at $5R_d$. The disc is represented by 4×10^6 particles. If we had used equal mass particles for the galactic disc, this would correspond to particle masses of $2500 M_\odot$. Such high masses would inhibit dynamical friction on objects of mass $\sim 10^4 M_\odot$, and lead to excessive heating of any infalling clusters. In order to reduce such effects, we use multimass disc particles, with masses ranging from $7 M_\odot$ within the inner 20 pc increasing to $1.2 \times 10^7 M_\odot$ in the disc's outskirts. Fig. 6 shows the distributions of masses and softening lengths of disc particles; the latter is related to particle mass via $\epsilon_p \propto m_p^{1/3}$. We use the epicyclic approximation to set Toomre- $Q = 1.2$. This set-up is imperfect and needs to be relaxed; moreover, simulations using such initial conditions can only be run for a few crossing times of the main disc, since the radial migration of stars induced by disc instabilities, including bars and spirals, would introduce massive particles to the central regions (Sellwood & Binney 2002; Debattista et al. 2006; Roškar et al. 2008). In order to check that

the system does not rapidly homogenize, we relaxed the system for 10 Myr, after which main disc particles in the central 100 pc have masses ranging from 7 to $2.8 \times 10^3 M_\odot$. In Fig. 7, we plot the mass distribution for the disc particles within the inner 100 pc at three different times for the longest merger simulation (M2, described below). The cumulative distribution (bottom panel) shows that the mass at the centre is dominated by particles with masses smaller than $2500 M_\odot$, with more than half the mass in this region coming from particles with masses less than $1000 M_\odot$.

4.2 Bulge model

On time-scales comparable to the crossing time of the galaxy, dynamical instabilities, such as bars and spirals, move particles to the central regions. Multimass particle simulations within discs therefore are no longer possible in these cases. We therefore set up a bulge, again neglecting the dark matter halo, and evolve the systems in this environment. The bulge model has a Hernquist (1990) profile:

$$\rho(r) = \frac{aM_b}{2\pi r(r+a)^3}, \quad (6)$$

where M_b is the bulge mass and a is the scale radius. We use $M_b = 5 \times 10^9 M_\odot$ and $a = 1.7$ kpc. The bulge is truncated by

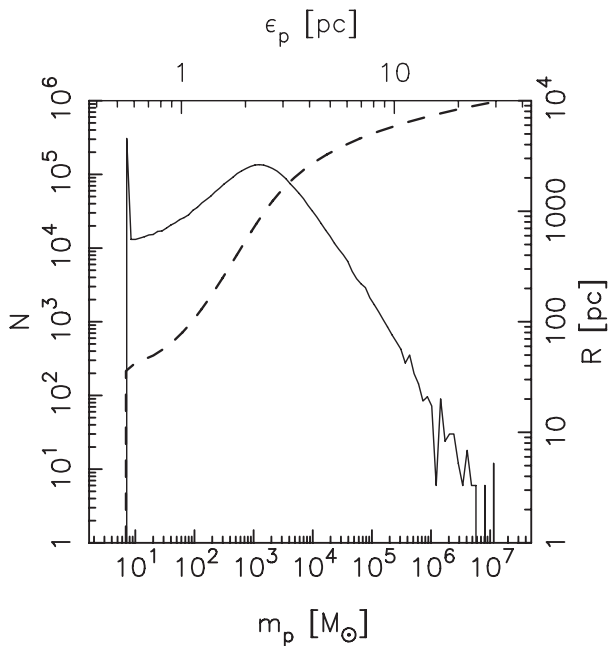


Figure 6. The unrelaxed initial conditions of the main galactic disc. The solid line shows the number of particles (left axis) and the dashed line the radius R (right axis) versus the particle mass (bottom axis) and versus softening ϵ (top axis).

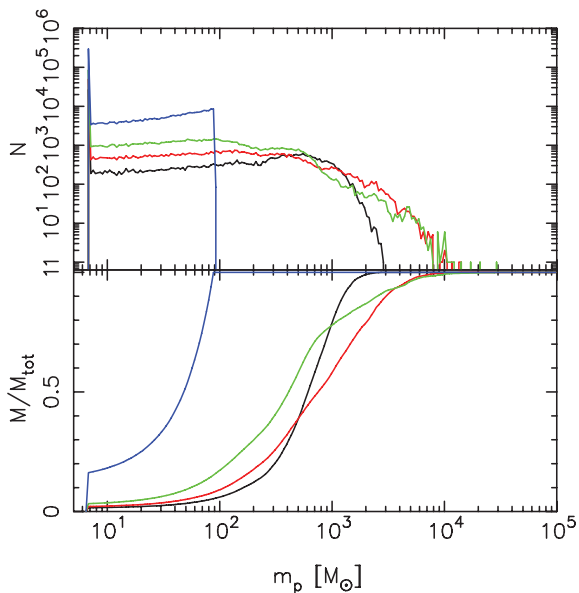


Figure 7. The masses of particles in the inner 100 pc of the main disc in run M2. Blue: initial set-up; black: initial conditions after relaxing the disc for 10 Myr; red: after 17.5 Myr; green: after 35 Myr. The top panel shows the number of particles of a given mass, while the bottom panel shows the cumulative mass distribution.

eliminating all particles with enough energy to reach $r > 15a$; therefore, the density drops gently to zero at this radius (Sellwood & Debattista 2009). The bulge is populated by 3.5×10^6 particles with masses ranging from 40 to $3.9 \times 10^5 M_\odot$; particle masses are selected by the weighting function $w(L) \propto 3 + 5000L^2$, with L the specific angular momentum, ensuring a high resolution within the inner 160 pc (Sellwood 2008). The softening is related to the particle mass via $\epsilon_p \propto m_p^{1/3}$. Unlike the disc, the bulge has no

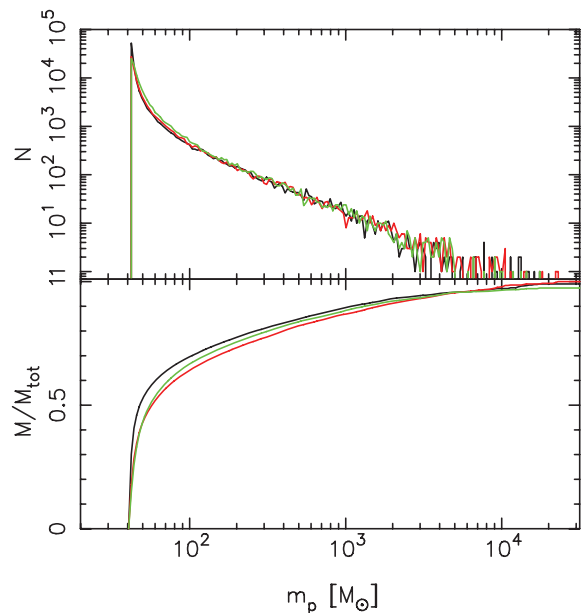


Figure 8. The masses of particles in the inner 30 pc of the bulge in simulation A1. Black: initial set-up; red: initial conditions after the 65 Myr needed for the infall of the NCS seed; green: after 0.275 Gyr. The top panel shows the number of particles of a given mass, while the bottom panel shows the cumulative mass distribution.

strong instabilities; therefore, the distribution of particles remains unchanged even on time-scales of a few Gyr. We need these time-scales to model multiple accretions of SCs. Fig. 8 shows the particles distribution for simulation A1, described below, within 32 pc at three different times. This simulation shows the largest changes in the mass distribution. Although accretion delivers higher mass particles into the central region, the distribution of particles does not change substantially.

4.3 Star cluster models

We set up model SCs, ranging in mass from 2×10^5 to $2 \times 10^6 M_\odot$, using an isotropic distribution function (DF): $f(x, v) = \mathcal{F}(E)$. The specific form we choose is a lowered polytrope DF

$$f(x, v) \propto [-2E(x, v)]^{n-3/2} - (-2E_{\max})^{n-3/2}, \quad (7)$$

with polytrope index $n = 2$ in all cases. We produce equilibrium models through the iterative procedure described in Debattista & Sellwood (2000). We set up five such models, C1–C5. All SC models have particles of equal mass ($1.1 M_\odot$ for C1–C2, $5.0 M_\odot$ for C3–C4 and $15 M_\odot$ for C5) and equal softening ($\epsilon = 0.104$ pc for C1 and C2, and $\epsilon = 0.13$ pc for C3–C5). IMBHs may be present in some SCs (Gebhardt et al. 2000; Gerssen et al. 2002, 2003; Gebhardt, Rich & Ho 2005; Noyola, Gebhardt & Bergmann 2008; Noyola et al. 2010, but see also van der Marel & Anderson 2010). In model C2, we include an IMBH at the centre of the cluster C1 by adiabatically growing the mass of a single particle with softening $\epsilon_p = 0.042$ pc over 100 Myr. Table 1 lists the properties of the SC models. The concentration c is defined as $c \equiv \log(R_{\text{eff}}/R_c)$, where R_{eff} is the half-mass radius (effective radius) and R_c is the core radius, where the surface density drops to half of the central. Fig. 9 plots the volume density profiles of the SCs. The central density ρ_0 ranges from 3×10^3 to $1 \times 10^5 M_\odot \text{pc}^{-3}$; the masses and R_{eff} (see Table 1) are comparable to young massive SCs in the Milky Way (Figer et al. 1999, 2002), in the Large Magellanic Cloud (Mackey &

Table 1. The SCs used in the simulations. M_* is the stellar mass of the SC, R_{eff} is the effective (half-mass) radius, c is the concentration (see text for definition) and M_{\bullet} is the mass of the black hole if one is present.

Model	M_* (M_{\odot})	R_{eff} (pc)	c	M_{\bullet} (M_{\odot})
C1	2.2×10^6	1.72	0.07	–
C2	2.2×10^6	1.60	0.07	4.4×10^4
C3	2.0×10^6	2.18	0.12	–
C4	2.0×10^5	1.11	0.12	–
C5	6.0×10^5	1.11	0.16	–

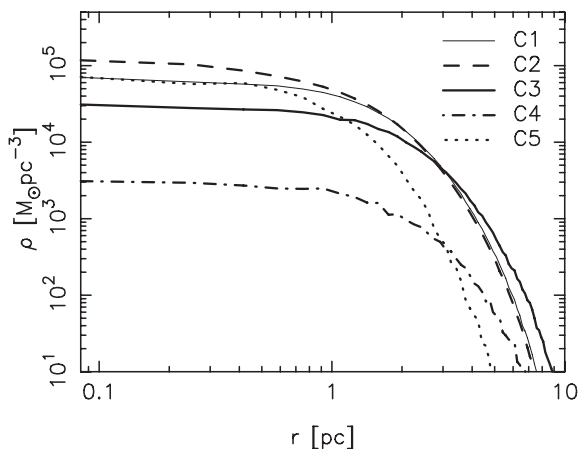


Figure 9. Volume density of the SC models C1–C5. The softening $\epsilon = 0.10$ pc for C1 and C2, and $\epsilon = 0.13$ pc for C3–C5.

Gilmore 2003), in the Fornax cluster (McLaughlin & van der Marel 2005), in irregular galaxies (Larsen, Brodie & Hunter 2004) and in interacting galaxies (Bastian et al. 2006).

4.4 Bare NCD model

If direct formation of a NCD via gas inflows precedes the full formation of a NC, how does the accretion of SCs alter the properties of such NCD? In order to mimic the dissipative formation of such a NCD, we introduce a stellar NCD at the centre of the bulge. We generated this NCD model by adiabatically growing a stellar disc component over a period of 0.5 Gyr. This NCD is exponential of the type in equation (5), with a scalelength $R_d = 9.5$ pc and scaleheight $z_d = 0.1R_d$. The disc, truncated at a radius of $5R_d$, consists of 2×10^5 particles each with softening $\epsilon = 0.13$ pc. The final total mass of the NCD is $1 \times 10^6 M_{\odot}$. We set the kinematics of the grown disc to give constant z_d and Toomre- $Q = 1.2$, as described in Debattista & Sellwood (2000). For this we, calculated the potential using a hybrid polar-grid code (Sellwood 2003).

4.5 Numerical parameters

All the simulations in this paper were evolved with PKDGRAV (Stadel 2001), an efficient, parallel tree-code. We used an opening angle $\theta = 0.7$ in all simulations. PKDGRAV is a multisteping code, with time-steps refined such that $\delta t = \Delta t/2^n < \eta(\epsilon/a)^{1/2}$, where ϵ is the softening and a is the acceleration at a particle's current position. We set $\eta = 0.1$ in all cases. Simulations A1–A3 used base time-step

$\Delta t = 10^5$ yr, whereas all other simulations used half this value $\Delta t = 0.5 \times 10^5$ yr.

5 RESULTS OF THE MERGER SIMULATIONS

We ran three simulations in which eight massive SCs were allowed to merge at the centre of the disc to form a NC. We use SC models C1 and C2 in these simulations because these SCs are sufficiently massive and concentrated to not evaporate too rapidly (McLaughlin & Fall 2008) and to have orbit decay times due to dynamical friction less than 3 Gyr from a radius of 1 kpc (Milosavljević 2004). The SCs were placed at random radii ranging from 14 to 92 pc and with velocities between 8 and 13 km s^{-1} , which are ~ 60 per cent of the local circular velocity. In run M1, the SCs are all initially in the mid-plane; in run M2 instead the SCs are vertically offset from the mid-plane by up to 67 pc, with tangential velocities similar to M1 and vertical velocities up to 1 km s^{-1} . Finally, run M3 is identical to run M1, but uses SC C2 instead of C1. Details of these simulations are listed in Table 2.

SCs merge after 13–36 Myr, with the longest time needed in M2. One SC failed to merge in run M1 and was excluded from all analysis.

5.1 Structural properties

We measured mass surface density profiles of the remnant NCs viewed face-on and obtained R_{eff} by fitting Sérsic or King profiles. The King profile clearly fits the profiles better, and we present results only of this fit throughout. The King profile is given by (King 1962)

$$\Sigma(R) = k \left(X^{-1/2} - C^{-1/2} \right)^2, \quad (8)$$

with normalization constant $k = \Sigma_0(1 - C^{-1/2})^{-2}$, $X(R, R_c) = 1 + (R/R_c)^2$ and $C(R_t, R_c) = 1 + (R_t/R_c)^2$, where R_c is the core radius and R_t is the tidal radius at which the projected density drops to zero. Integration yields the cumulative form of the King profile for $R \leq R_t$:

$$M(R) = \pi R_c^2 k \left(\ln X - 4 \frac{X^{1/2} - 1}{C^{1/2}} + \frac{X - 1}{C} \right), \quad (9)$$

which is the mass in projection within a cylinder of radius R . R_{eff} can be approximated by

$$R_{\text{eff}} = R_c \left[e^{(M/2\pi R_c^2 k) - 1} \right]^{1/2}. \quad (10)$$

The merger remnants have R_{eff} in the range 4.3–4.7 pc with mass fractions from 87–97 per cent of the total *merged* SC mass. These masses are consistent with those of observed NCs (Geha, Guhathakurta & van der Marel 2002; Böker et al. 2004; Côté et al. 2006; Seth et al. 2006; Walcher et al. 2006). Fig. 10 plots the mean

Table 2. The merger simulations. $N(\text{SC})$ gives the number of SCs used and column SC lists which SCs from those in Table 1 are used in the simulation. Column Host shows which host galaxy model is used as initial conditions.

Run	$N(\text{SC})$	SC	Host	Comments
M1	8	C1	Disc	SCs at mid-plane of main disc
M2	8	C1	Disc	Six SCs offset from main disc mid-plane
M3	8	C2	Disc	SCs at mid-plane of main disc
A1	10	C5	Bulge	Multiple accretion of SCs on to NCS
A2	20	C4	Bulge	Accretion of SCs on to a NCD
A3	20	C4	Bulge	Like A2 with 50 per cent retrograde orbits

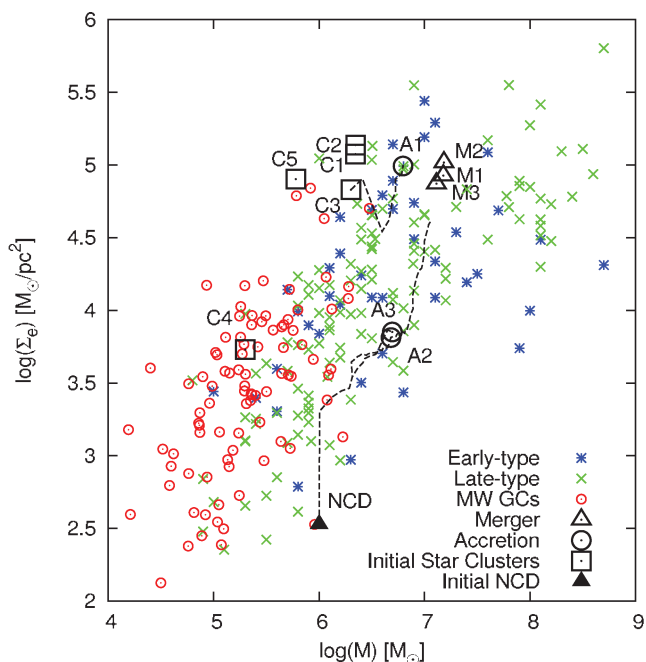


Figure 10. Comparison of the simulated and observed NCs in the plane spanned by the mean surface density within R_{eff} versus total NC mass. We compare with the observed NCs of early-type (blue stars) and late-type spiral galaxies (green crosses) as well as Milky Way GCs (red open circles). The initial SCs are shown by the open black squares, while the remnant NCs are shown by black open triangles for multiple mergers and by black open circles for multiple accretions. The initial NCD is shown by a filled black triangle. The tracks of the evolving NC in the multiple accretion simulations are indicated by dashed lines.

surface density within R_{eff} versus the total mass of the merger remnants and compares them to NCs in early-type galaxies (Côté et al. 2006), late-type spiral galaxies (Carollo et al. 1997; Carollo, Stiavelli & Mack 1998; Carollo et al. 2002; Böker et al. 2002; Seth et al. 2006) and Milky Way GCs (Walcher et al. 2005). As shown by Capuzzo-Dolcetta & Mocchi (2008b), we find that SC mergers produce remnants which have structural properties in good agreement with observed NCs.

As was shown already by Bekki et al. (2004), the merger remnants can be triaxial. We measured the ellipticities viewed face-on and edge-on of the simulated NCs using equation (4), obtaining the isophote at R_{eff} using the task ELLIPSE in IRAF. The NC in M1 is significantly non-axisymmetric, with face-on mean ellipticity $\varepsilon_{\text{FO}} \simeq 0.37$. We also measured the 3D shape using the moment-of-inertia tensor as described in Debattista et al. (2008). Fig. 11 plots the density axial ratios and triaxiality, $T = (a^2 - b^2)/(a^2 - c^2)$ (Franx, Illingworth & de Zeeuw 1991), of the remnant NCs. In run M1, the NC is triaxial within $2R_{\text{eff}}$. Models M2 and M3 explore two ways of producing more axisymmetric NCs. In M2, we start the SCs off the mid-plane. This makes the NC oblate, with $\varepsilon_{\text{FO}} \simeq 0.05$. In run M3 instead we add 2 per cent IMBHs to the SCs which again results in an oblate NC, also with $\varepsilon_{\text{FO}} \simeq 0.03$.

We find remnant edge-on ellipticities at $3R_{\text{eff}}$ in the range $\varepsilon_{\text{EO}} = 0.36\text{--}0.56$. These values are consistent with the range of observed ellipticities 0.39–0.89 (Seth et al. 2006).

Fig. 12 shows B_4 for the edge-on view. In the triaxial NC of M1, B_4 varies with viewing angle but is always negative, i.e. the NC is boxy. The NCs in M2 and M3 are also boxy. The merger of SCs

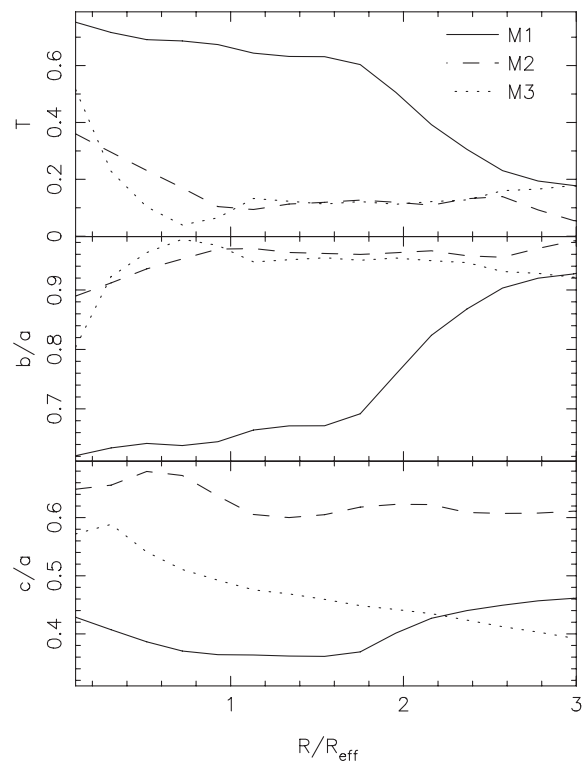


Figure 11. The 3D shape of the NC in runs M1 (solid lines), M2 (dashed lines) and M3 (dotted lines). The top panel shows the triaxiality T , the second row b/a and the third c/a .

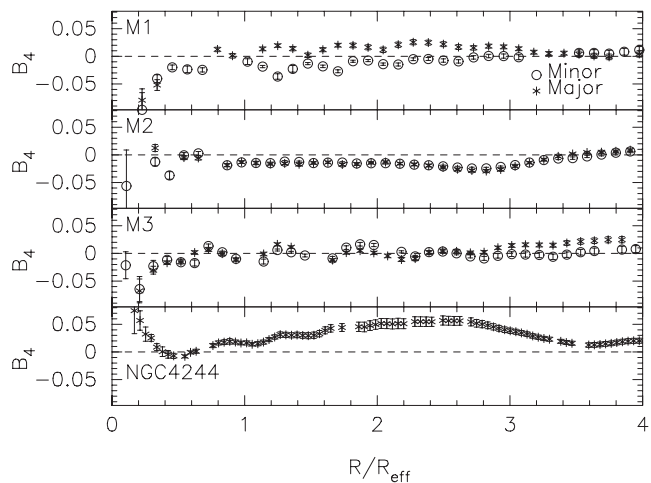


Figure 12. The B_4 parameter for the merger simulations. From top to bottom, these are M1, M2, M3 and the NC of NGC 4244 for comparison. The remnant NCs have $B_4 \lesssim 0$, whereas the observed NC in NGC 4244 has clearly discy isophotes, i.e. positive B_4 .

cannot produce isophotes as discy as observed in the NC of NGC 4244.

5.2 Remnant kinematics

Bekki et al. (2004) found that his merger remnants were rotating, while Capuzzo-Dolcetta & Mocchi (2008a) found that merger remnants are kinematically distinct from the main disc/bulge.

Fig. 13 shows the edge-on line-of-sight kinematics of the remnant NCs. They are all clearly strongly rotating. However, the second

moment of the velocity, V_{rms} , shows that the merger remnants are so dominated by dispersion at the centre that V_{rms} is centrally peaked, contrary to what is seen in the NC of NGC 4244 (Fig. 4). In the bottom row, we show the rotation curve $V_c(R)$, the line-of-sight velocity $V(x)$, the line-of-sight velocity dispersion $\sigma(x)$ and the root-mean-square (rms) velocity $V_{\text{rms}}(x)$ of the merger remnants. Velocities in M1–M3 peak at larger radii than those observed in NGC 4244 and M33 (see Fig. 1).

In Fig. 14, the anisotropies $\beta_\phi = 1 - \sigma_\phi^2/\sigma_R^2$ (top panel) and $\beta_z = 1 - \sigma_z^2/\sigma_R^2$ (bottom panel) show that the remnant NCs are all radially biased within $4R_{\text{eff}}$. M2 is less radially biased than M3, which may seem surprising at first, but the radius of the sphere of influence of the IMBH in M3 is less than 1 pc, explaining the absence of a tangential bias at R_{eff} . The vertical pressure support is generally smallest. The initial vertical energy of the SCs in run M2 imparts larger vertical random motions, leading to the smallest

β_z and smallest edge-on ellipticity ε_{EO} . Radial anisotropy has been noted in the past as a signature of the merging process (e.g. Burkert & Naab 2005; Bournaud, Jog & Combes 2007; Debattista et al. 2008; Thomas et al. 2009). The presence of plausible IMBHs does not alter this result.

5.3 Accretion on to super star clusters

The superstar cluster (SSC) found by Kornei & McCrady (2009) in the nuclear region of NGC 253 seems destined to fall into the centre of the galaxy and form the basis of a NC. How would the accretion of further SCs alter the structure and kinematics of such a seed NC? Observed Milky Way GCs are found to be nearly isotropic (Gebhardt 1994; Gebhardt et al. 1995). How much mass needs to be accreted to appreciably alter the isotropic distribution? In run A1, we study the accretion of SCs on to a NCS by introducing a

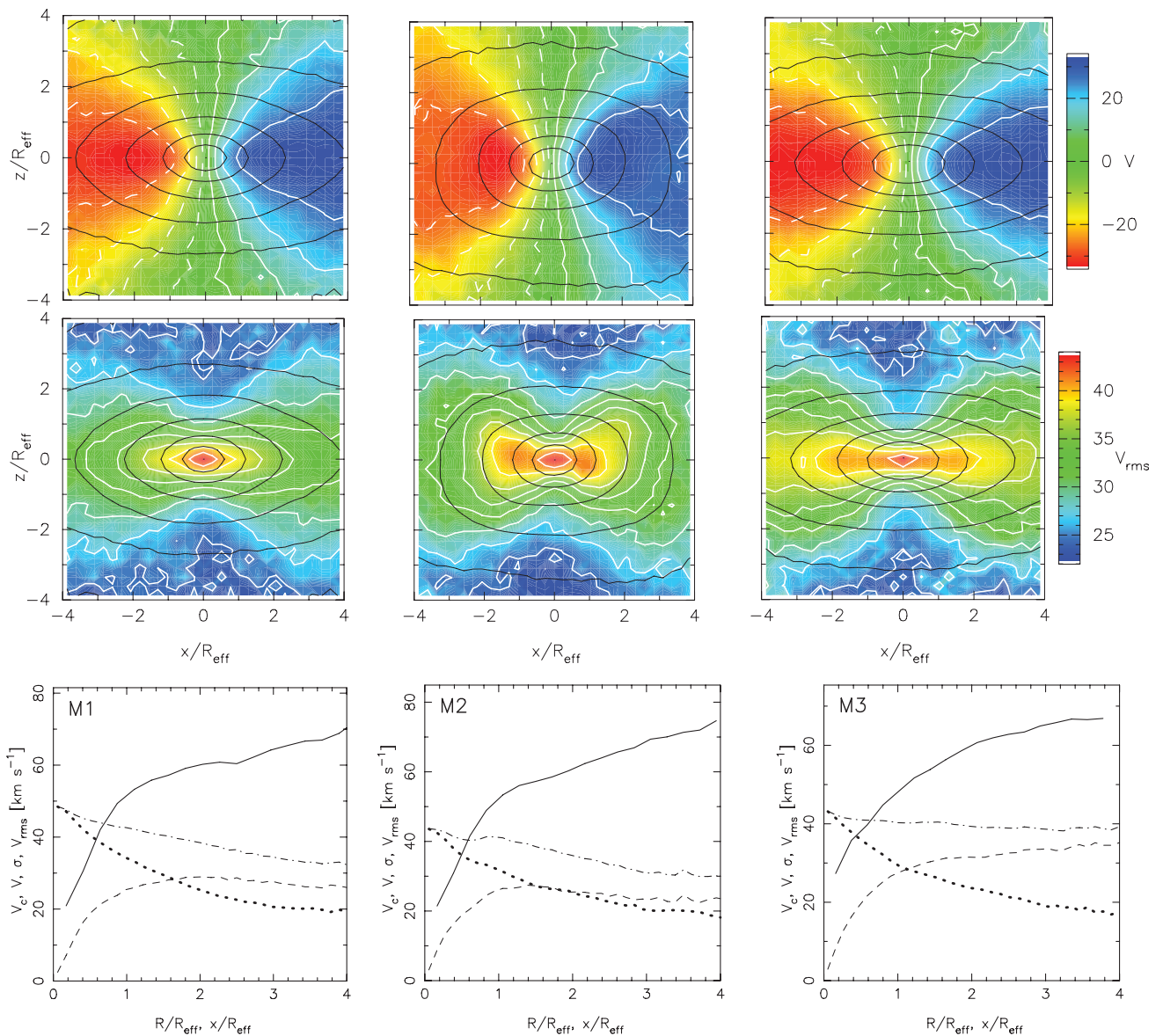


Figure 13. Velocity (top row) and V_{rms} (middle row) fields within $4R_{\text{eff}}$ for M1 (left), M2 (middle) and M3 (right). The velocity fields show a large-scale rotation. In all cases, V_{rms} is centrally peaked. In the top two rows, black contours show log-spaced density with intervals of 0.1 of the central density, while the white contours show the kinematic contours corresponding to each panel. The bottom row plots the rotation curve $V_c(R)$ (solid lines), the line-of-sight velocities $V(x)$ (dashed lines), the line-of-sight velocity dispersions $\sigma(x)$ (dotted lines) and the rms velocities $V_{\text{rms}}(x)$ (dot-dashed lines) along the major axis.

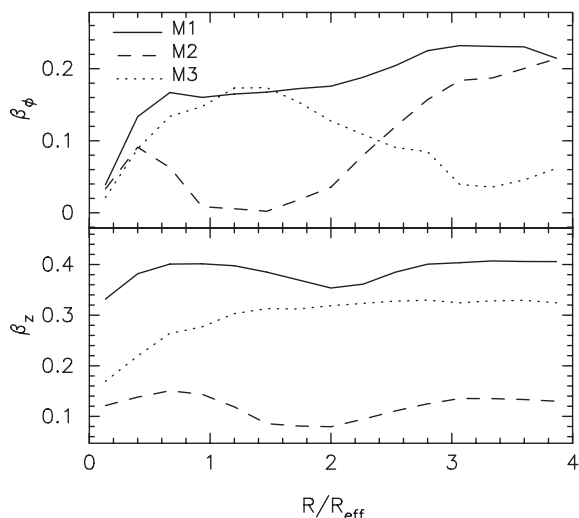


Figure 14. Final anisotropy β_ϕ (top) and β_z (bottom) in runs M1, M2 and M3.

spherical isotropic SC inside the bulge model. We form the NCS by letting a massive SC fall to the centre. We used SC C3 and started it at 127 pc on a circular orbit, allowing it to settle at the centre over 65 Myr, before we start the accretion of 10 SCs. We use model C5 for the accreted SCs, starting them on circular orbits at a distance of 32 pc from the centre. In total, the mass accreted corresponds to ~ 3 times the NCS's initial mass. Each accretion is allowed to finish before a new SC is inserted. A single accretion on average requires ~ 20 Myr. Table 2 gives further details of this simulation.

After each accreted SC, we measure R_{eff} by fitting a King profile (equation 8) to the mass surface density profile of the NC. The final remnant has $R_{\text{eff}} \sim 3.2$ pc and structural properties consistent with observed NCS, as shown in Fig. 10, which tracks the evolving NC. The NC becomes triaxial after it has doubled in mass. The final $\varepsilon_{\text{FO}} \simeq 0.17$ and $\varepsilon_{\text{EO}} \simeq 0.51$; the latter is in the observed range (Seth et al. 2006). The final triaxiality $T \simeq 0.4$. Fig. 15 shows that the remnant NC in A1 is discy ($B_4 > 0$).

Multiple accretion of young SCs allows us to also explore the effect of a different M/L for a *young* accreted SC. For the NC in NGC 4244, the structural properties are obtained from I -band

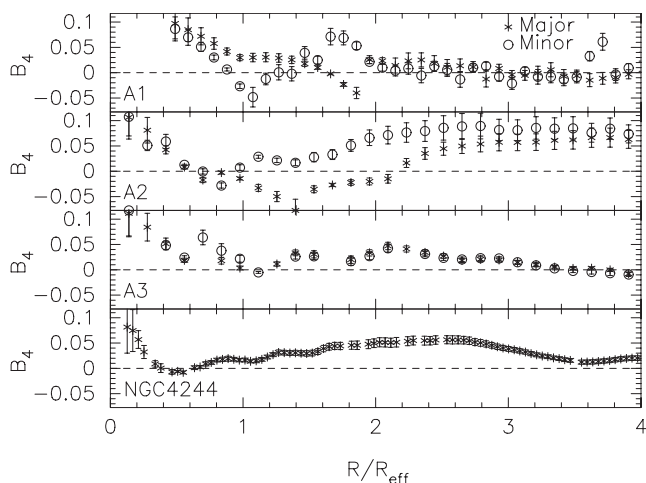


Figure 15. B_4 for edge-on projections of runs A1, A2 and A3 compared with the NC in NGC 4244 (bottom). For the simulations, we measured the isophotes along the edge-on semiprincipal axes.

observations (Seth et al. 2006) and the kinematics from K -band data (Seth et al. 2008b). Therefore, we obtain both the M/L in the I and K bands for the NCD assuming a single stellar population with an age of about 70 Myr and a metallicity of $[\text{Fe}/\text{H}] = -0.4$ and for the NCS assuming two stellar populations, the first with an age of 1 Gyr with the same metallicity and the second of 10 Gyr and a metallicity of $[\text{Fe}/\text{H}] = -1.4$ in NGC 4244. Using the stellar evolution code of Maraston (1998, 2005), this gives $M/L \approx 0.2$ for the NCD and $M/L \approx 1.6$ for the NCS in the I band and $M/L \approx 0.1$ for the NCD and $M/L \approx 0.8$ for the NCS in the K band. Throughout the rest of this paper, we adopt the M/L values in the I band for the analysis of structural properties and M/L values in the K band for the kinematics, assuming that stars from the last accreted SC are young, while the rest of the stars are old, to obtain a luminosity weighting. Adopting these M/L values, the final edge-on ellipticity becomes $\varepsilon_{\text{EO}} \simeq 0.56$.

We produce a luminosity-weighted density map of the final NC and fit two components, an elliptical King profile and an exponential disc profile, as in Seth et al. (2006), to measure the structural properties of the NCS and NCD component. While the NCS has $R_{\text{eff}} \sim 3.2$ pc and a flattening $\varepsilon \sim 0.59$, we did not fit a reasonable NCD.

The initial SSC is isotropic and has no rotation and remains unrotating after falling to the centre. Fig. 16 shows the evolution of $(V/\sigma)_e$; after the first accretion, the merger remnant's rotation has already increased to $(V/\sigma)_e \simeq 0.23$. By the end of the simulation, the mass-weighted $(V/\sigma)_e \simeq 0.34$ ($\simeq 0.41$ luminosity weighted). The velocity field of the remnant, seen in Fig. 17, shows that the NC is rotating. However, V_{rms} is still dominated by the velocity dispersion at the centre even when luminosity weighting. The line-of-sight velocity V peaks at larger radii than observed in NGC 4244 and M33.

The settling of the SC to the centre does not change its dispersion within R_{eff} , since the bulge mass within R_{eff} changes only by about 0.6 per cent. The evolution of β_ϕ and β_z is shown in Fig. 18. The first accretion drives β_ϕ to negative values which slowly increases as more mass is accreted. The final β_z peaks within R_{eff} and declines further out.

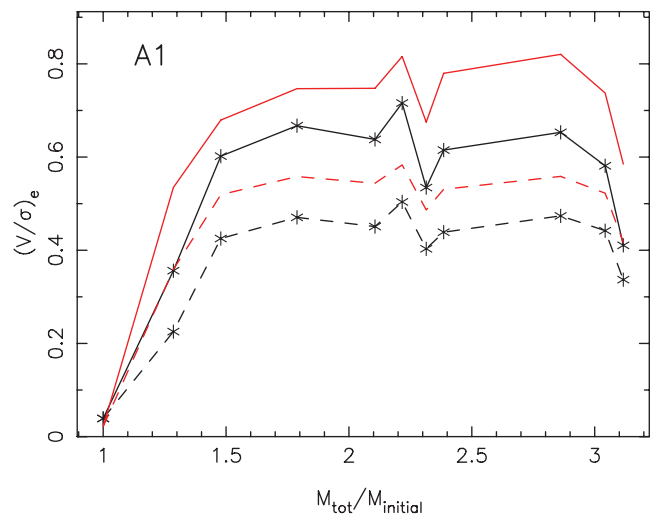


Figure 16. The evolution of $(V/\sigma)_e$ in run A1 within R_{eff} (black lines) and $3R_{\text{eff}}$ (red lines). The dashed lines represent mass-weighted and the solid lines luminosity-weighted measurements as described in the text.

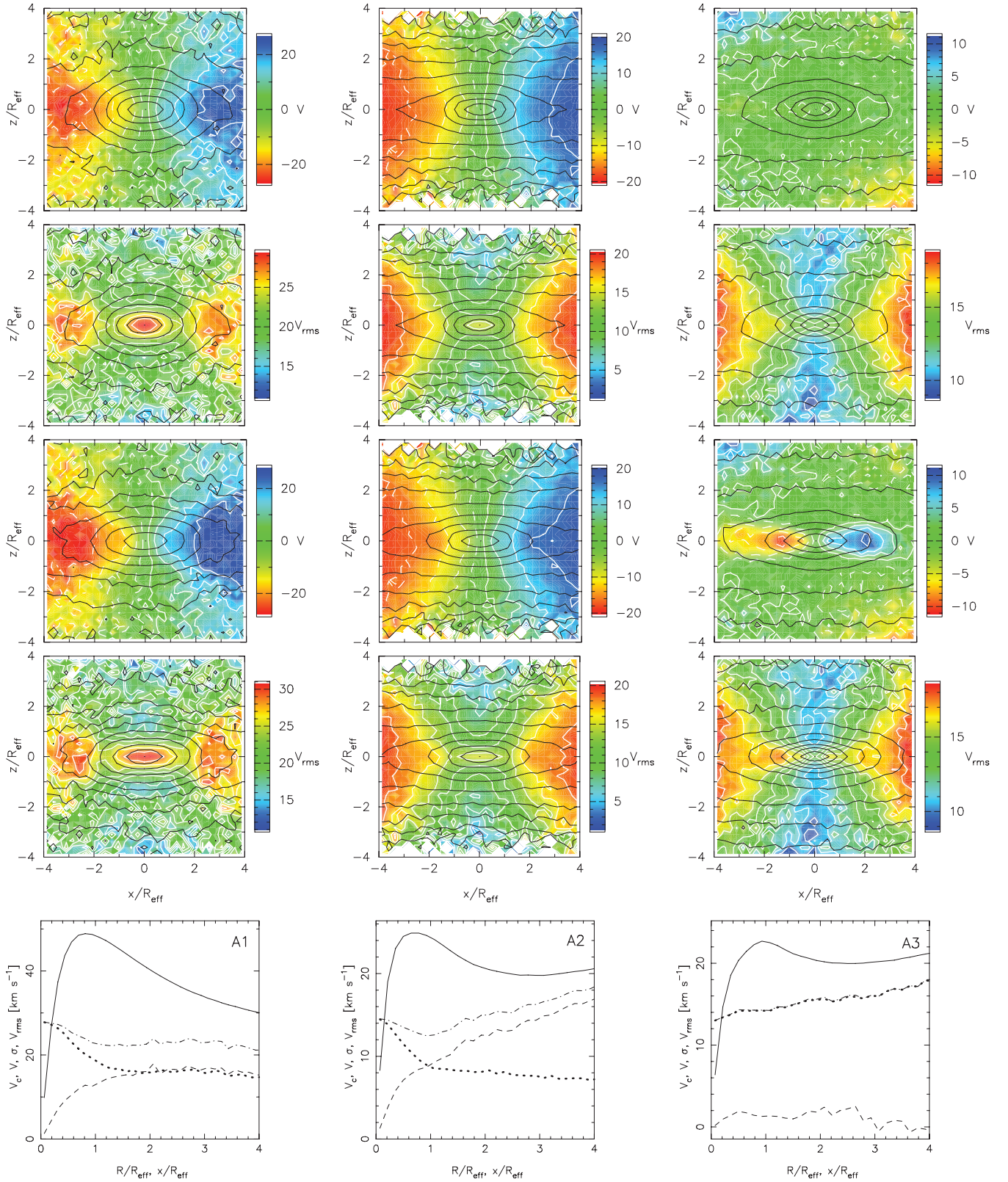


Figure 17. Kinematic fields for the accretion simulations A1 (left), A2 (middle) and A3 (right). The top two rows adopt a mass weighting, while the next two rows use luminosity weighting, as described in the text. In the top four rows, the black contours show log-spaced density with intervals of 0.1 of the central density, while the white contours show the kinematic contours corresponding to each panel. Run A3 shows significant rotation only with luminosity weighting. The bottom row shows the rotation curve $V_c(R)$ (solid lines), the line-of-sight velocities $V(x)$ (dashed lines), the line-of-sight velocity dispersions $\sigma(x)$ (dotted lines) and the rms velocities $V_{\text{rms}}(x)$ (dot-dashed lines) along the major axis.

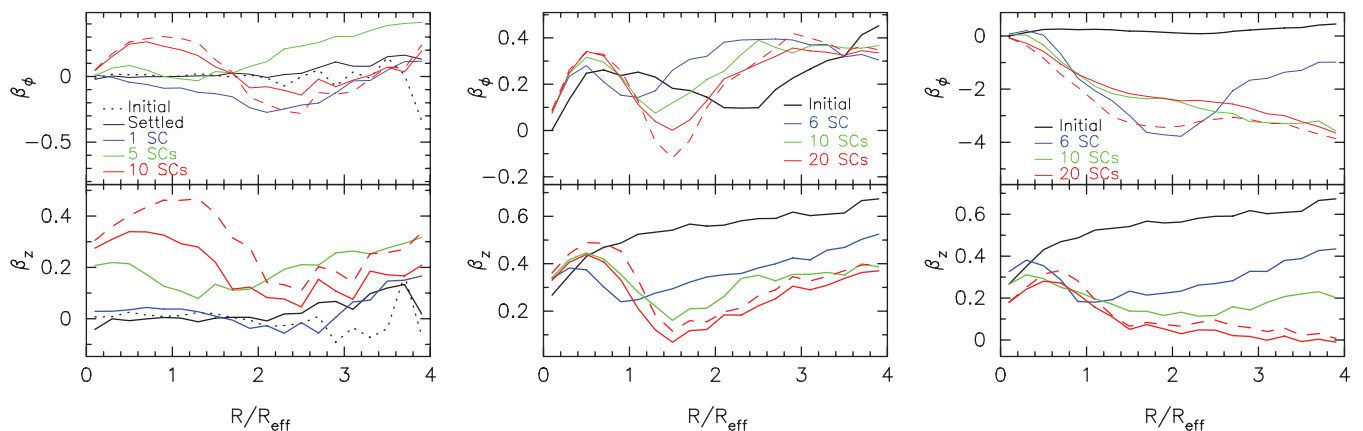


Figure 18. The anisotropies β_ϕ (top) and β_z (bottom) after different accretion events for runs A1 (left), A2 (middle) and A3 (right); note the different scales in the ordinates. For A1, we show the initial SSC by the black dotted line. For each simulation, the red dashed lines show the luminosity-weighted anisotropies of the final NC. The lack of net angular momentum in run A3 drives β_ϕ to negative values, even when luminosity weighting, whereas in run A2, β_ϕ is positive.

6 ACCRETION ON TO BARE NCDs

Here we consider the case of a bare NCD, without an initial NCS, accreting multiple young SCs. The initial NCD component has a mass of $1 \times 10^6 M_\odot$. We use model C4 to represent the infalling SCs, placing them at 63 pc from the centre of the NC, since the NCD is barely affected by the SC until it is well within this radius. In run A2, all SCs are on prograde circular orbits, whereas in A3 half of the SCs have retrograde orbits. In total, the NCD accretes 20 SCs, corresponding to four times its own mass. All SCs orbit in the plane of the NCD without any vertical motions. Each accretion event requires 20–30 Myr to complete; we allow each accretion to finish before introducing the next SC. In total, these simulations require 1.1 Gyr. Table 2 gives further details of these simulations.

The remnants have both $R_{\text{eff}} \simeq 11.1$ pc and structural properties consistent with observed NCs as shown in Fig. 10, which tracks the evolving NC. The surface density increases after each accretion event, evolving along the track of observed NCs. When we continue to grow the NC in A2 by accreting a further 30 SCs, the NC becomes denser than the infalling SCs and the surface density continues to increase. Fig. 19 shows the surface density profiles seen edge-on. The top panels show mass-weighted maps of the surface density. In the middle row of Fig. 19, we present luminosity-weighted surface density maps, which are more discy than the mass-weighted ones. In the bottom panel of Fig. 19, we show the surface density profiles.

Like the merger remnants, the accretion remnants are generally triaxial. The NC in run A2 is triaxial with a final $\varepsilon_{\text{FO}} \simeq 0.22$ and a $T \simeq 0.4$, whereas run A3 is rounder with $\varepsilon_{\text{FO}} \simeq 0.05$ and $T \simeq 0.1$. The final edge-on ellipticity at $3R_{\text{eff}}$ is $\varepsilon_{\text{EO}} \simeq 0.60$ for run A2 and $\varepsilon_{\text{EO}} \simeq 0.56$ for run A3 and a luminosity-weighted ellipticity $\varepsilon_{\text{EO}} \simeq 0.73$ in A2 and $\varepsilon_{\text{EO}} \simeq 0.66$ in A3, which is in agreement with observed NCs. Accretion leads to the formation of NCs with discy isophotes at large radii as can be seen in Fig. 15. As in NGC 4244, they show an increase in B_4 towards the centre and a decline further out. Unlike the merger of SCs in simulations M1–M3, the multiple accretion of SCs in runs A1 and A2 result into NCs with discy isophotes, because in these simulations all SCs are accreted within the same plane.

The vertical density profile of the NC in run A2 at R_{eff} is shown in Fig. 20. The NCD is vertically heated by the accretion of SCs. The last accreted SC is distributed in a thinner component than the initial NCD. We again fit the luminosity-weighted density map with

an elliptical King profile and an exponential disc profile as in Seth et al. (2006). This gives a NCS with $R_{\text{eff}} \sim 9.8$ pc and a flattening of $q \sim 0.37$ and a NCD with $z_0 \sim 1.7$ pc and a scalelength $R_d \sim 3.3$ pc. The fitted NCD accounts for 2 per cent of the NC mass, which is ~ 3 times smaller than in NGC 4244. The scaleheight and scalelength of the NCD in run A2 is about the same as that observed in NGC 4244. Thus, structurally, the NC is comparable to that in NGC 4244, provided that the accreted SC is young.

The initial NCD is strongly rotating. Accretion reduces the rotation of the remaining NC. Fig. 21 shows the evolution of $(V/\sigma)_e$. The first accretion leads to a large decrease in $(V/\sigma)_e$. In run A2, the subsequent accretions induce smaller changes, quickly asymptoting to $(V/\sigma)_e \simeq 0.45$ ($\simeq 0.52$ luminosity weighted). $(V/\sigma)_e$ increases with radius regardless of which weighting is used. Run A3 instead drops to $(V/\sigma)_e \simeq 0.10$ although a luminosity weighting gives the appearance of more rotation, $(V/\sigma)_e \simeq 0.40$, comparable to that in run A2.

Fig. 17 plots the first two moments of the line-of-sight kinematics. The remnant NC in A2 is significantly rotating, while that in A3 shows rotation only when luminosity weighted. The V shown in the bottom panel of Fig. 17 peaks at larger radii compared to those in NGC 4244 and M33. Unlike in runs M1–M3 and A1, the NC remnant in runs A2 and A3 has V_{rms} that increases with radius, like the NC of NGC 4244. However, the V_{rms} profiles in Fig. 17 shows that in run A2, V_{rms} increases within R_{eff} . In Fig. 22, we show that V_{rms} develops a central peak within R_{eff} after the initial NCD has doubled its mass. This leads us to conclude that NGC 4244 cannot have accreted more than half of its mass as stars.

6.1 The vertical anisotropy

As usual for rapidly rotating discs, the initial NCD is radially biased, with β_z initially large, but this decreases with accretion, although it remains positive. Unlike with the kinematic measurements, no important differences in β_z and β_ϕ occur if we weight by luminosity as shown in Fig. 21. Regardless of whether mass or luminosity weighting is applied, β_z peaks within R_{eff} and declines beyond.

The JAM model of the NC in NGC 4244 has a $\beta_z \simeq -0.2$. We have shown in model M2 that accretion of SCs with vertical motions decreases β_z . In run A2, the accreted SCs are in the plane of the initial NCD. In further tests, we let the NC in A2 accrete

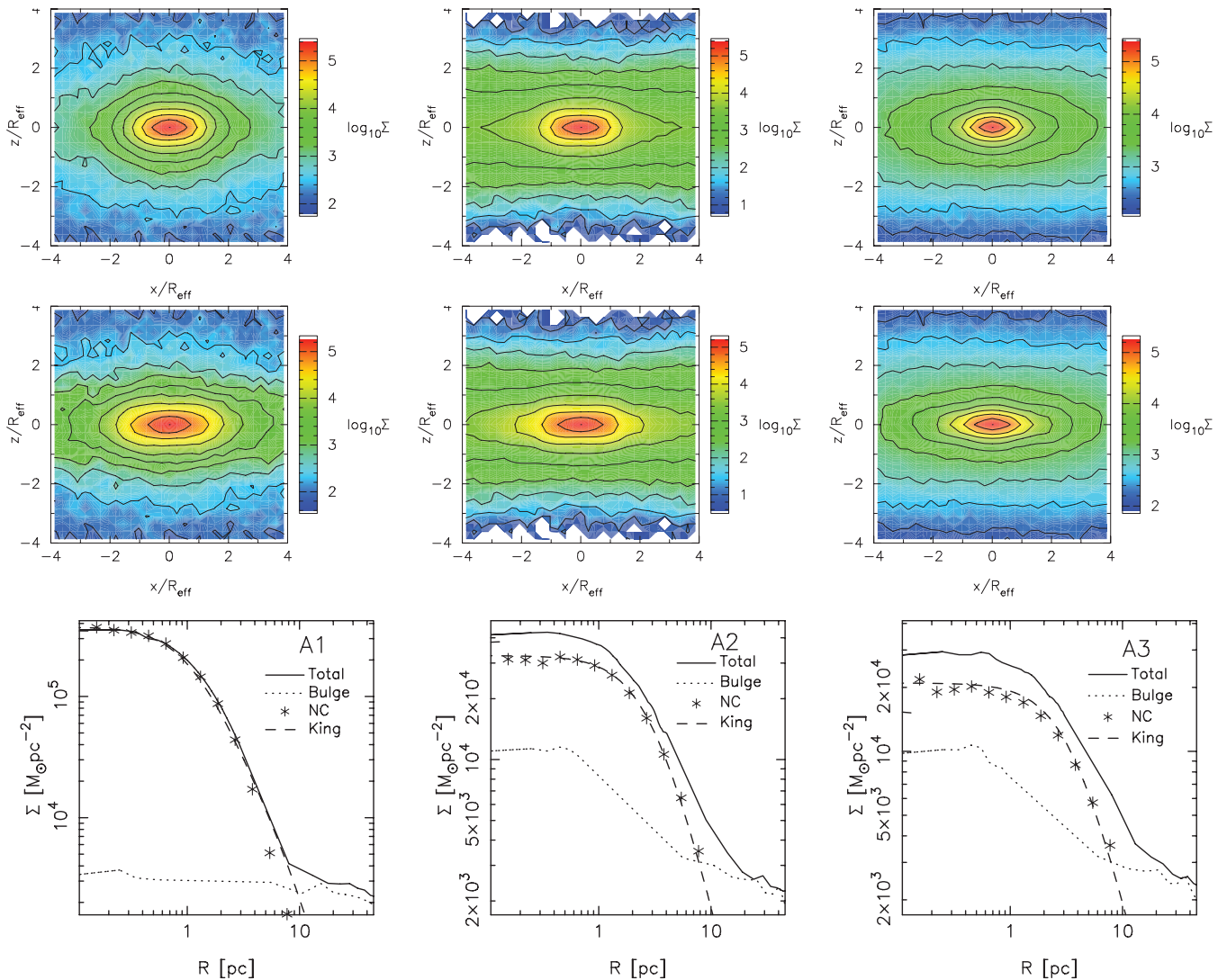


Figure 19. Projected surface density maps seen edge-on for simulations A1 (left), A2 (middle) and A3 (right). The top row shows mass-weighted maps and the middle row luminosity-weighted ones. In both rows, black contours show log-spaced density with intervals of 0.1 of the central density. In the bottom panel, we show the face-on surface density profiles measured within circular annuli for the NC as stars and the corresponding King profile by a dashed line. The bulge is shown by the dotted line and the combined surface density by the solid line.

the 20th SC on a polar orbit using SC models C4, C5 and C3 ($M = 2 \times 10^5$, 6×10^5 , $2 \times 10^6 M_\odot$). In Fig. 23, we show the anisotropy β_ϕ and β_z of the remaining NC after these accretions. Modest accretion off the plane of the disc drives β_z to negative values within R_{eff} . The accretion of SC C3 drives $\beta_z < 0$ within $4R_{\text{eff}}$, and it also leads to $\beta_\phi < 0$ within R_{eff} . The accretion of SC C5 causes $\beta_z < 0$ within R_{eff} and $\beta_\phi < 0$ only within $< 0.5R_{\text{eff}}$. Thus the negative β_z , which the JAM model finds in NGC 4244, requires that the NC accretes at least ~ 10 per cent of its mass directly as stars.

7 JAM MODELS OF SIMULATED NCs

To compare the rotation of real NCs and the simulated ones in a fully consistent way, we applied the same JAM approach to the simulated NCs. The MGE models were fitted to reconstructed images of all models listed in Table 2 at an edge-on orientation, for different viewing directions in the disc plane. For each projection, we fitted the anisotropy β_z and M/L of the simulated NCs, and we

then measured the rotation parameter κ at the best-fitting $(\beta_z, M/L)$. The inferred parameters are given in Table 3 and compared with the values measured from the particles. The comparison shows that the simple JAM models capture the global anisotropy of the simulated NCs of the merger simulations and gives confidence in the values we extracted from the real data. In summary for all simulations, as with the observations, we measure a degree of rotation $\kappa \approx 1$ within 5 per cent for models M1 and M2, and within 10 per cent for model M3. Given the complex accretion process of the NC, it is remarkable for the rotation to be so closely linked to the NC shape. This result is similar to what was found for real galaxies in Cappellari (2008) and suggests that a general process may be responsible for both observations. For the models of the merger simulations, we recover a weak anisotropy, with models for M1 and M3 anisotropic with $\beta_z \approx 0.25$ and ≈ 0.17 , respectively, while model M2 is closer to fully isotropic with $\beta_z \approx 0.04$ within $3R_{\text{eff}}$. Contrary to models M1–M3, the JAM models do not represent acceptable models for the accretion simulations A1–A3. In fact, the kinematics predicted from the simulated photometry under the assumption of constant M/L and

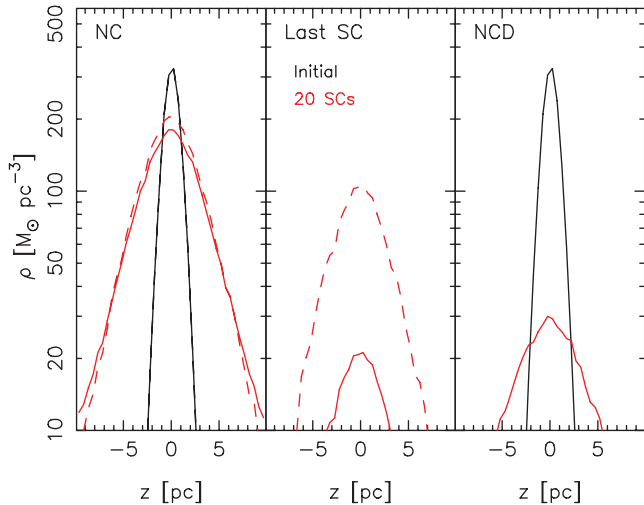


Figure 20. The vertical density profile of simulation A2 for the initial NC (black) and after 20 accreted SCs (red). The solid lines show mass-weighted and the dashed lines luminosity-weighted profiles. We plot the density profile for the total NC, the last accreted SC and the particles of the initial NCD in the left-hand, middle and right-hand panels, respectively.

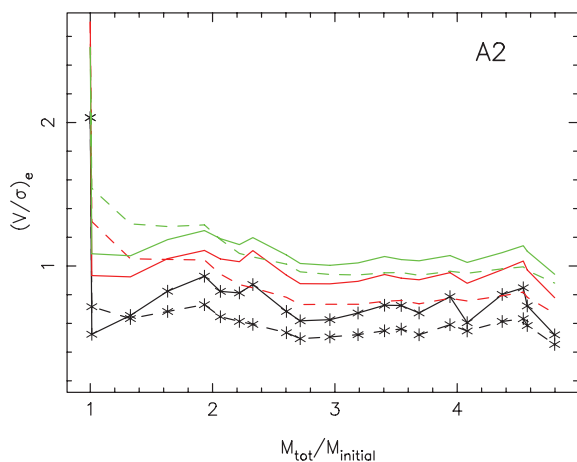


Figure 21. The evolution of the $(V/\sigma)_e$ within R_{eff} (black lines), $3R_{\text{eff}}$ (red lines) and $5R_{\text{eff}}$ (green lines) in run A2. The dashed lines represent mass-weighted and the solid lines luminosity-weighted measurements adopting the M/L of the NCS and NCD in NGC 4244.

an oblate velocity ellipsoid are qualitatively quite different from the simulated one. The main reason for this discrepancy is the strong variation in the M/L in the simulated NC, which is not included in the JAM models. Although it would be easy to construct JAM models using the gravitational potential directly measured from the simulations, this cannot be easily done from the observations. However, in all accretion simulations, the global rotation can robustly be determined by JAM.

We perform an independent measure of the degree of rotation of the simulated NCs using equations (3) and (4) to place the simulations M1–M3 and A1–A3 on the $(V/\sigma, \varepsilon)$ diagram. For the NCs M1–M3, the diagram provides results consistent with the JAM models, for both simulated and observed NCs. In particular, both models M1 and M3 are in a location of the diagram which indicates significant anisotropy, while model M2 and the observed NC of M33 and NGC 4244 are close to the isotropic line (with a typical uncertainty of ~ 0.1). The measured values are shown in Fig. 5. To first order,

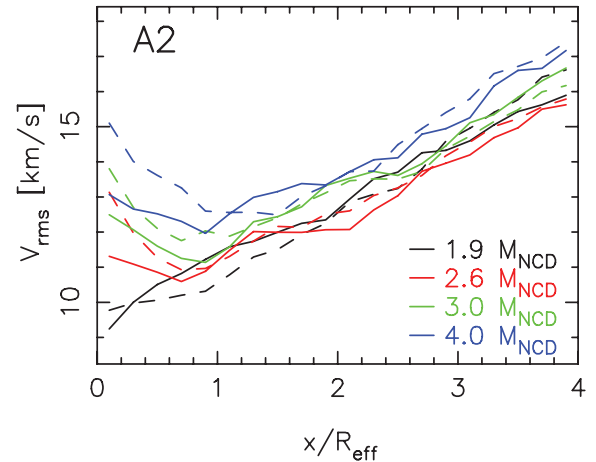


Figure 22. The V_{rms} profile after the NC has grown to 1.9 times (black lines), 2.6 times (red lines), 3.0 times (green lines) and 4.0 times (blue lines) the initial NCD's mass. The solid lines show the $V_{\text{rms}}(x)$ of the NC seen side-on and the dashed lines seen end-on.

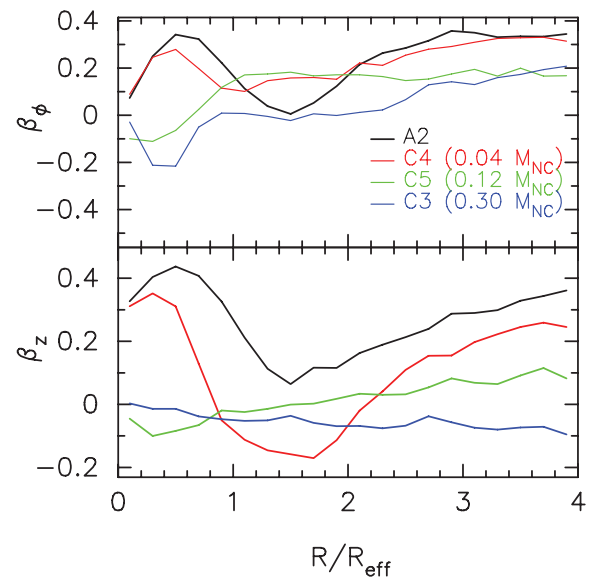


Figure 23. The anisotropies β_ϕ (top) and β_z (bottom) for run A2 after the accretion of 20 SCs and for the three test runs if we replace the final accreted SC with the indicated SC on a polar orbit.

the diagram shows that both the simulated clusters and the real ones are rapidly rotating. The simulated NCs in runs M1 and M3 are flatter than M2, but they have a similar $(V/\sigma)_e$. The NCs in the accretion simulations A1–A3 are as flat as the merger simulations M1 and M3. They have comparable $(V/\sigma)_e$, although in A3 only the last accreted SC causes the rotation. All these results are consistent with the finding of the JAM models.

8 DISCUSSION AND CONCLUSIONS

8.1 *In situ* formation versus accretion

We have examined in detail the formation of NCs via the mergers of SCs. This has been proposed as an important avenue for NC formation (Tremaine et al. 1975; Miocchi et al. 2006; Capuzzo-Dolcetta & Miocchi 2008a; Agarwal & Milosavljević 2011). The main support for this mechanism comes from the similarity of

Table 3. Global cylindrical anisotropy and parameters from the JAM models for the simulations and observations. We also present the values measured directly from the simulations.

Run	JAM			Simulation	
	β_z	κ	ε_{EO}	$\langle\beta_\phi\rangle$	$\langle\beta_z\rangle$
M1	0.25	0.94	0.55	0.15	0.38
M2	0.04	0.99	0.37	0.08	0.10
M3	0.17	0.90	0.56	0.17	0.26
A1	–	–	0.56	0.05	0.35
A2	–	–	0.73	0.10	0.31
A3	–	–	0.66	–1.92	0.20
NGC 4244	–0.2	1.06	0.43		
M33	0.0	0.84	0.28		

scaling relations between SCs and NCs (Lotz et al. 2001; Walcher et al. 2005). In agreement with previous studies (Bekki et al. 2004; Capuzzo-Dolcetta & Mocchi 2008a,b), we find that such scaling relations are preserved after mergers.

As with previous studies (Bekki et al. 2004), the merger of SCs was found to produce triaxial NCs, but we showed that axisymmetry can result from the presence of IMBHs or sufficient vertical motions. In the only observed galaxy where the face-on shape can be determined, M33, we showed that the NC is most likely axisymmetric. When the simulated NCs are viewed edge-on, mergers produce boxy NCs, unless the merger of SCs occurs on to a pre-existing SSC or a pre-existing NCD at the centre. In all simulated NCs, the flattening is in the range observed for NCs in edge-on galaxies (Seth et al. 2006).

Our simulations indicate that a NC formed via merging of cored SCs leads to a cored NC (Dehnen 2005). During the merger, the NC density and mass increase, and the NC evolves along the track defined by the observed density–mass relation for NCs. The increase in density does not saturate. The accretion of SCs leads to growth in mass, size and mean density of the NC. As seen in Fig. 10, observed NCs and Milky Way GCs overlap in the range $10^2 < \Sigma_e < 10^5 M_\odot \text{pc}^{-2}$. Some observed NCs are denser than the present-day Milky Way GC population. Studies of young massive SCs in interacting galaxies (Whitmore & Schweizer 1995; McCrady & Graham 2007) show that they have similar masses (10^5 – $10^6 M_\odot$) and similar sizes as the Milky Way GCs (Bastian et al. 2006, and references therein). Due to the smaller infall times of massive SCs (Milosavljević 2004; Neumayer et al. 2011), the mergers of these massive SCs are more likely. Thus, if the main formation mechanism of NCs is the accretion of SCs, it would explain why NCs are denser than the present-day GC population.

Observed NCs contain thin, blue discs of young (<100 Myr) stars. In NGC 4244, the mass of this disc is about 5 per cent of the total NC mass – if this is typical for the lifetime of a galaxy, then over a Hubble time dissipation and star formation is sufficient to build the NC (Seth et al. 2006). On the other hand, we have shown that even if the accreted SCs confer no net angular momentum to the NC, because the last accreted young SC dominates the luminosity, the apparent rotation can be quite large. We found that mergers can produce rapidly rotating NCs having $(V/\sigma)_e$ values as large as those observed (Seth et al. 2008b). However, the second moment of the LOSVD, V_{rms} , is centrally peaked, unlike in the observations. It is only if we introduce a rapidly rotating $[(V/\sigma)_e \simeq 2.0]$ nuclear disc at the centre of the initial system that the subsequent evolution produced by infalling SCs is able to qualitatively reproduce the

observed V_{rms} field as well as the observed isophotal shape, degree of rotation and mass–density relation, provided no more than half of the NC’s mass is accreted. Thus a pure merger origin of NCs can be excluded.

Our JAM model of the NC in NGC 4244 has $\beta_z = -0.2$. Because Cappellari (2008) found that a decrease in inclination leads to an increase in β_z , we tested the effect of inclination on β_z for the JAM model of NGC 4244. For inclinations $>75^\circ$, we found β_z continues to be negative at a 3σ level. Thus the $\beta_z < 0$ in NGC 4244 cannot be a projection effect and must be intrinsic. However, a NCD formed out of gas cooling would have $\beta_z > 0$. For example, the JAM model of the NC in NGC 404 has $\beta_z \sim 0.5$ (Seth et al. 2010); in this case, the observed burst of star formation ~ 1 Gyr ago could easily have fed its NC and given rise to its positive β_z . By scattering box orbits, central black holes can lower β_z (e.g. Merritt & Quinlan 1998). Whereas Seth et al. (2008a) find indirect evidence of SMBHs, with masses ranging from 10 to 100 per cent in ~ 10 per cent of NCs, in NGC 4244 the radius of influence for the largest possible IMBH is <1 pc, while the NC has $R_{\text{eff}} = 5$ pc. Therefore, the presence of an IMBH in the centre of NGC 4244 cannot explain its $\beta_z < 0$. The only way we were able to produce $\beta_z < 0$ was through the accretion of SCs on highly inclined orbits. Thus, at least ~ 10 per cent of the mass of the NC of NGC 4244 needs to be accreted as SCs in order to obtain $\beta_z < 0$, which constitutes a lower limit on the amount of mass accreted in the form of SCs.

8.2 Nuclear cluster formation in dwarf elliptical galaxies

Our simulations can also make testable predictions relating to the formation of nuclei in dE galaxies. Lotz et al. (2001) suggested that NCs in dE galaxies could have formed by the merger of GCs. They found a depletion of the most massive GCs relative to the less massive ones in the inner region of galaxies. They interpreted this as being due to shorter dynamical friction infall time-scales for massive GCs than for the lower mass ones. In the ACS Virgo Cluster Survey, Côté et al. (2006) found that, on average, NCs in dE galaxies are 3.5 mag brighter than the mean GC. Therefore, if NCs form via the merger of GCs, on average about 25 GCs need to merge. Similar to what we found for NCs in late-type spiral galaxies (Fig. 10), Côté et al. (2006; see their fig. 18) found that the NCs are denser than the mean density of the GC population in dE galaxies. They also found that the fraction of red GCs and the $(g - z)_{\text{AB}}$ colour of NCs increases with the host galaxy luminosity (Côté et al. 2006; Peng et al. 2006). Using Monte Carlo simulations, and assuming that these NCs formed via mergers, Côté et al. (2006) found that the resulting scaling relation of the NC’s colours is less steep than those observed. From spectroscopic data, Paudel, Lisker & Kuntschner (2011) found that the metallicity of NCs in a sample of dE galaxies correlates with the luminosity of the host galaxy. They also found that the median difference in age between the NC and the galactic main body is about ~ 3.5 Gyr and that the difference is more prominent in dEs with discy isophotal shapes. This implies that the formation of NCs in dEs might be enhanced by the accretion of gas. In contrast, Paudel et al. (2011) found fairly old and metal-poor NCs in very faint dEs, resembling the properties of the GC population. This suggests that NCs in faint dEs might have formed by different processes than the NCs in brighter dEs.

In summary, both the accretion of gas with *in situ* star formation and the merger of GCs could be at work to form NCs in dE galaxies. If NCs in dEs form via merger of GCs, our simulations indicate that they will have boxy shapes, have centrally peaked V_{rms} and be radially biased. On the other hand, if the main formation mechanism

is dissipation, NCs will have discy isophotes and no centrally peaked V_{rms} . At present, no available observational data exist which are able to test these predictions.

8.3 The $M_{\text{CMO}}-\sigma_e$ relation

The star formation histories in NCs of late-type spiral galaxies are extended, with the youngest population of stars less than 100 Myr old (Rossa et al. 2006; Walcher et al. 2006; Seth et al. 2010). NCs appear to be offset from the $M_{\bullet}-\sigma_e$ relation of SMBHs (Ferrarese et al. 2006a; Wehner & Harris 2006). NCs have the same slope, but, for a given velocity dispersion σ_e , are 10 times more massive than SMBHs. McLaughlin et al. (2006) found that this offset can be explained by feedback from stars and supernovae. Our simulations indicate that at least 10 per cent of the mass of NCs needs to be accreted by SCs and that at least 50 per cent of its mass needs to be accreted as gas. Therefore, a fraction of the star formation could occur outside the NC. However, the accreted SCs have to be young and therefore still formed within the central region. SCs with masses in a range of $10^5-10^6 M_{\odot}$ have to be formed within 60–200 pc, otherwise their infall times are longer than 100 Myr. Therefore, even if the NC has accreted half of its mass in young SCs, stellar feedback occurs within the central region of the galaxy and therefore remains a plausible explanation for the $M_{\text{NC}}-\sigma_e$.

8.4 Summary

We have studied the formation and evolution of stellar NCs using N -body simulations. Our main conclusions can be summarized as follows.

(i) We find no evidence of non-axisymmetry in the NC of M33. Its PA is consistent with that of its main disc, and its apparent ellipticity is consistent with a vertical flattening $q = 0.7$, which is the average observed in the NCs of edge-on late-type galaxies (Seth et al. 2006). There is also only a small misalignment between the photometric and kinematic PAs. While this is the only galaxy where this measurement can be done at present, it suggests that NCs are generally axisymmetric.

(ii) The NC in NGC 4244 is nearly isotropic, with $\beta_z = -0.2 \pm 0.1$, and is rapidly rotating. It has a mass of $(1.1 \pm 0.2) \times 10^7 M_{\odot}$; if an IMBH is present, its mass is less than 1 per cent that of the NC. It is not possible from these models to distinguish whether the rotation is present throughout the NC or is restricted to the NCD.

(iii) Mergers of SCs produce NCs with density and sizes consistent with observations, evolving along the track of observed NCs. The growth of the mean density does not saturate and continues to grow with further accretion of SCs. Remnant NCs can be axisymmetric. Multiple accretions of young SCs on to a pre-existing NCS can also produce discy isophotal shapes. Mergers can lead to rapidly rotating NCs, as observed. They have $\beta_z \lesssim 0.4$, where initial vertical motions induce the smallest value. However, these NCs have centrally peaked V_{rms} unlike observed NCs in late-type discs.

(iv) Accretion of young SCs on to a bare NCD produces NCs with densities, sizes and ellipticities comparable to those observed. They show discy isophotes and have rotations comparable to those in the NCs of NGC 4244 and M33. However, V_{rms} is dominated by dispersion if the accreted mass is greater than the initial mass of the NCD. Therefore, gas accretion is needed for the formation of NCs in late-type spiral galaxies. The formation of the NC in NGC 4244

requires at least 50 per cent of the mass to be accreted as gas to match the observations.

(v) The negative β_z in the NC of NGC 4244 requires at least ~ 10 per cent its total mass to have been accreted from SCs in highly inclined orbits.

(vi) We caution that even if the accreted SCs do not impart any net angular momentum, the last accreted SC can dominate the apparent rotation when luminosity weighting and could be similar to the $(V/\sigma)_e$ and V_{rms} fields of observed NCs.

(vii) In general, the simulations indicate that if NCs form via the merger of GCs, they will have boxy shapes, have centrally peaked V_{rms} and be radially biased. If the main formation mechanism of NC formation is dissipation, they will have discy isophotes and no centrally peaked V_{rms} . While V_{rms} profiles constrain the fraction of dissipation, the anisotropy of the NC constrains the fraction of accretion of stars.

(viii) With the results presented in this paper, the simulations are now ahead of the observations with predictions of detailed observables that can be used to constrain the formation scenarios better. Integral-field observations of the kinematics of more NCs are essential for further progress, and we hope these will be obtained in the near future.

ACKNOWLEDGMENTS

Part of the simulations in this paper were performed on the COSMOS Consortium supercomputer within the DIRAC Facility jointly funded by STFC, the Large Facilities Capital Fund of BIS. Simulations have also been run at the Arctic Region Supercomputing Center (ARSC) and the High Performance Computer Facility at the University of Central Lancashire. We thank Jerry Sellwood for providing us with the multi-mass bulge model and Jakob Walcher for providing us with his observational data. MH thanks Chris Brook and Rok Roškar for their support and help. MC acknowledges support from a Royal Society University Research Fellowship. We thank Nate Bastian and the anonymous referee for constructive comments.

REFERENCES

- Agarwal M., Milosavljević M., 2011, *ApJ*, 729, 35
 Andersen D. R., Walcher C. J., Böker T., Ho L. C., van der Marel R. P., Rix H.-W., Shields J. C., 2008, *ApJ*, 688, 990
 Bastian N., Saglia R. P., Goudfrooij P., Kissler-Patig M., Maraston C., Schweizer F., Zoccali M., 2006, *A&A*, 448, 881
 Bekki K., 2007, *Publ. Astron. Soc. Australia*, 24, 77
 Bekki K., Couch W. J., Drinkwater M. J., Shioya Y., 2004, *ApJ*, 610, L13
 Bender R., 1988, *A&A*, 193, L7
 Binney J., 1978, *MNRAS*, 183, 501
 Binney J., 2005, *MNRAS*, 363, 937
 Binney J., Tremaine S., 2008, *Galactic Dynamics*, 2nd edn. Princeton Univ. Press, Princeton, NJ
 Binney J. J., Davies R. L., Illingworth G. D., 1990, *ApJ*, 361, 78
 Böker T., Laine S., van der Marel R. P., Sarzi M., Rix H.-W., Ho L. C., Shields J. C., 2002, *AJ*, 123, 1389
 Böker T., Sarzi M., McLaughlin D. E., van der Marel R. P., Rix H.-W., Ho L. C., Shields J. C., 2004, *AJ*, 127, 105
 Bournaud F., Jog C. J., Combes F., 2007, *A&A*, 476, 1179
 Burkert A., Naab T., 2005, *MNRAS*, 363, 597
 Cappellari M., 2002, *MNRAS*, 333, 400
 Cappellari M., 2008, *MNRAS*, 390, 71
 Cappellari M., Emsellem E., 2004, *PASP*, 116, 138
 Cappellari M. et al., 2007, *MNRAS*, 379, 418
 Cappellari M. et al., 2011, *MNRAS*, 269

- Capuzzo-Dolcetta R., Mocchi P., 2008a, *ApJ*, 681, 1136
 Capuzzo-Dolcetta R., Mocchi P., 2008b, *MNRAS*, 388, L69
 Carollo C. M., Stiavelli M., de Zeeuw P. T., Mack J., 1997, *AJ*, 114, 2366
 Carollo C. M., Stiavelli M., Mack J., 1998, *AJ*, 116, 68
 Carollo C. M., Stiavelli M., Seigar M., de Zeeuw P. T., Dejonghe H., 2002, *AJ*, 123, 159
 Corbelli E., Schneider S. E., 1997, *ApJ*, 479, 244
 Côté P. et al., 2006, *ApJS*, 165, 57
 Debattista V. P., Sellwood J. A., 2000, *ApJ*, 543, 704
 Debattista V. P., Mayer L., Carollo C. M., Moore B., Wadsley J., Quinn T., 2006, *ApJ*, 645, 209
 Debattista V. P., Moore B., Quinn T., Kazantzidis S., Maas R., Mayer L., Read J., Stadel J., 2008, *ApJ*, 681, 1076
 Dehnen W., 2005, *MNRAS*, 360, 892
 Eliche-Moral M. C., Balcells M., Aguerri J. A. L., González-García A. C., 2006, *A&A*, 457, 91
 Emsellem E., van de Ven G., 2008, *ApJ*, 674, 653
 Emsellem E., Monnet G., Bacon R., 1994, *A&A*, 285, 723
 Emsellem E. et al., 2011, *MNRAS*, 414, 888
 Ferrarese L. et al., 2006a, *ApJ*, 644, L21
 Ferrarese L. et al., 2006b, *ApJS*, 164, 334
 Figier D. F., McLean I. S., Morris M., 1999, *ApJ*, 514, 202
 Figier D. F. et al., 2002, *ApJ*, 581, 258
 Franx M., Illingworth G., de Zeeuw T., 1991, *ApJ*, 383, 112
 Gebhardt K., 1994, PhD thesis, Rutgers, The State University
 Gebhardt K., Pryor C., Williams T. B., Hesser J. E., 1995, *AJ*, 110, 1699
 Gebhardt K., Pryor C., O'Connell R. D., Williams T. B., Hesser J. E., 2000, *AJ*, 119, 1268
 Gebhardt K., Rich R. M., Ho L. C., 2005, *ApJ*, 634, 1093
 Geha M., Guhathakurta P., van der Marel R. P., 2002, *AJ*, 124, 3073
 Gerhard O. E., 1993, *MNRAS*, 265, 213
 Gerssen J., van der Marel R. P., Gebhardt K., Guhathakurta P., Peterson R. C., Pryor C., 2002, *AJ*, 124, 3270
 Gerssen J., van der Marel R. P., Gebhardt K., Guhathakurta P., Peterson R. C., Pryor C., 2003, *AJ*, 125, 376
 Goerdt T., Moore B., Kazantzidis S., Kaufmann T., Macciò A. V., Stadel J., 2008, *MNRAS*, 385, 2136
 Goerdt T., Moore B., Read J. I., Stadel J., 2010, *ApJ*, 725, 1707
 Grant N. I., Kuipers J. A., Philipps S., 2005, *MNRAS*, 363, 1019
 Hernquist L., 1990, *ApJ*, 356, 359
 Hubble E. P., 1926, *ApJ*, 64, 321
 Illingworth G., 1977, *ApJ*, 218, L43
 Jedrzejewski R. I., 1987, *MNRAS*, 226, 747
 King I., 1962, *AJ*, 67, 471
 Kormendy J., Bender R., 1996, *ApJ*, 464, L119
 Kormendy J., Djorgovski S., 1989, *ARA&A*, 27, 235
 Kornei K. A., McCrady N., 2009, *ApJ*, 697, 1180
 Krajnović D., Cappellari M., de Zeeuw P. T., Copin Y., 2006, *MNRAS*, 366, 787
 Larsen S. S., Brodie J. P., Hunter D. A., 2004, *AJ*, 128, 2295
 Lauer T. R., Faber S. M., Ajhar E. A., Grillmair C. J., Scowen P. A., 1998, *AJ*, 116, 2263
 Li Y., Haiman Z., Mac Low M.-M., 2007, *ApJ*, 663, 61
 Lotz J. M., Telford R., Ferguson H. C., Miller B. W., Stiavelli M., Mack J., 2001, *ApJ*, 552, 572
 Lotz J. M., Miller B. W., Ferguson H. C., 2004, *ApJ*, 613, 262
 McCrady N., Graham J. R., 2007, *ApJ*, 663, 844
 Maciejewski W., Teuben P. J., Sparke L. S., Stone J. M., 2002, *MNRAS*, 329, 502
 Mackey A. D., Gilmore G. F., 2003, *MNRAS*, 340, 175
 McLaughlin D. E., Fall S. M., 2008, *ApJ*, 679, 1272
 McLaughlin D. E., van der Marel R. P., 2005, *ApJS*, 161, 304
 McLaughlin D. E., King A. R., Nayakshin S., 2006, *ApJ*, 650, L37
 Maraston C., 1998, *MNRAS*, 300, 872
 Maraston C., 2005, *MNRAS*, 362, 799
 Merritt D., 2009, *ApJ*, 694, 959
 Merritt D., Quinlan G. D., 1998, *ApJ*, 498, 625
 Milosavljević M., 2004, *ApJ*, 605, L13
 Mocchi P., Capuzzo Dolcetta R., Di Matteo P., Vicari A., 2006, *ApJ*, 644, 940
 Naab T., Burkert A., 2003, *ApJ*, 597, 893
 Naab T., Burkert A., Hernquist L., 1999, *ApJ*, 523, L133
 Naab T., Khochfar S., Burkert A., 2006, *ApJ*, 636, L81
 Navarro J. F., Frenk C. S., White S. D. M., 1996, *ApJ*, 462, 563
 Neumayer N., Walcher C. J., Andersen D., Sánchez S. F., Böker T., Rix H.-W., 2011, *MNRAS*, 413, 1875
 Noyola E., Gebhardt K., Bergmann M., 2008, *ApJ*, 676, 1008
 Noyola E., Gebhardt K., Kissler-Patig M., Lützgendorf N., Jalali B., de Zeeuw P. T., Baumgardt H., 2010, *ApJ*, 719, L60
 Paudel S., Lisker T., Kuntschner H., 2011, *MNRAS*, 413, 1764
 Peng E. W. et al., 2006, *ApJ*, 639, 95
 Read J. I., Goerdt T., Moore B., Pontzen A. P., Stadel J., Lake G., 2006, *MNRAS*, 373, 1451
 Read J. I., Lake G., Agertz O., Debattista V. P., 2008, *MNRAS*, 389, 1041
 Roškar R., Debattista V. P., Quinn T. R., Stinson G. S., Wadsley J., 2008, *ApJ*, 684, L79
 Rossa J., van der Marel R. P., Böker T., Gerssen J., Ho L. C., Rix H.-W., Shields J. C., Walcher C.-J., 2006, *AJ*, 132, 1074
 Satoh C., 1980, *PASJ*, 32, 41
 Schinnerer E., Böker T., Meier D. S., 2003, *ApJ*, 591, L115
 Schinnerer E., Böker T., Meier D. S., Calzetti D., 2008, *ApJ*, 684, L21
 Scott N. et al., 2009, *MNRAS*, 398, 1835
 Sellwood J. A., 2003, *ApJ*, 587, 638
 Sellwood J. A., 2008, *ApJ*, 679, 379
 Sellwood J. A., Binney J. J., 2002, *MNRAS*, 336, 785
 Sellwood J. A., Debattista V. P., 2009, *MNRAS*, 398, 1279
 Seth A. C., Dalcanton J. J., de Jong R. S., 2005, *AJ*, 129, 1331
 Seth A. C., Dalcanton J. J., Hodge P. W., Debattista V. P., 2006, *AJ*, 132, 2539
 Seth A., Agüeros M., Lee D., Basu-Zych A., 2008a, *ApJ*, 678, 116
 Seth A. C., Blum R. D., Bastian N., Caldwell N., Debattista V. P., 2008b, *ApJ*, 687, 997
 Seth A. C. et al., 2010, *ApJ*, 714, 713
 Shlosman I., Begelman M. C., 1989, *ApJ*, 341, 685
 Stadel J. G., 2001, PhD thesis, Univ. Washington
 Thomas J. et al., 2009, *MNRAS*, 393, 641
 Tremaine S. D., Ostriker J. P., Spitzer L., Jr, 1975, *ApJ*, 196, 407
 van der Marel R. P., 1991, *MNRAS*, 253, 710
 van der Marel R. P., Anderson J., 2010, *ApJ*, 710, 1063
 van der Marel R. P., Franx M., 1993, *ApJ*, 407, 525
 van der Marel R. P., van Dokkum P. G., 2007, *ApJ*, 668, 738
 van der Wel A., van der Marel R. P., 2008, *ApJ*, 684, 260
 Wagner S. J., Bender R., Moellenhoff C., 1988, *A&A*, 195, L5
 Walcher C. J. et al., 2005, *ApJ*, 618, 237
 Walcher C. J., Böker T., Charlot S., Ho L. C., Rix H.-W., Rossa J., Shields J. C., van der Marel R. P., 2006, *ApJ*, 649, 692
 Wehner E. H., Harris W. E., 2006, *ApJ*, 644, L17
 Whitmore B. C., Schweizer F., 1995, *AJ*, 109, 960
 Zaritsky D., Elston R., Hill J. M., 1989, *AJ*, 97, 97

This paper has been typeset from a $\text{\TeX}/\text{\LaTeX}$ file prepared by the author.